Iron transport pathways in the human malaria parasite *Plasmodium falciparum* revealed by RNA-sequencing

Juliane Wunderlich[1,2,*], Vadim Kotov[2], Lasse Votborg-Novél[1], Christina Ntalla[1], Maria Geffken[3], Sven Peine[3], Silvia Portugal[1], Jan Strauss[2,#]

[1] Max Planck Institute for Infection Biology (MPIIB), 10117 Berlin, Germany
[2] Centre for Structural Systems Biology (CSSB), 22607 Hamburg, Germany
[3] University Medical Center Hamburg-Eppendorf (UKE), Institute of Transfusion Medicine, 20246 Hamburg, Germany

* Correspondence: juliane.wunderlich@mail.mcgill.ca, Current address: Robert Koch Institute, Department of Infectious Disease Epidemiology, 13353 Berlin, Germany

[#] Current address: German Maritime Centre, 20457 Hamburg, Germany

ORCiD:

Juliane Wunderlich	0000-0002-5818-5488
Lasse Votborg-Novél	0000-0003-0381-0669
Sven Peine	0000-0002-6365-9916
Silvia Portugal	0000-0003-4567-9101
Jan Strauss	0000-0002-6208-791X

Keywords: *Plasmodium falciparum*, malaria, drug target, iron deficiency, transporters, nutrient uptake, gene expression, AlphaFold.

ABSTRACT

Host iron deficiency is protective against severe malaria as the human malaria parasite *Plasmodium falciparum* depends on free iron from its host to proliferate. Due to the absence of transferrin, ferritin, ferroportin, and a functional heme oxygenase, the parasite's essential pathways of iron acquisition, storage, export, and detoxification differ from those in humans and may thus be excellent targets for therapeutic development. However, the *P. falciparum* proteins involved in these processes remain largely unknown.

Here, we show that parasites cultured in erythrocytes from an iron-deficient donor displayed significantly reduced growth rates compared to those grown in red blood cells from healthy controls. Sequencing of parasite RNA revealed diminished expression of genes involved in overall metabolism, hemoglobin digestion, and metabolite transport under low-iron versus control conditions. Supplementation with hepcidin, a specific ferroportin inhibitor, resulted in increased free iron levels in erythrocytes, enhanced parasite replication, and transcriptional upregulation of genes responsible for merozoite motility and host cell invasion. Based on endogenous GFP tagging of differentially expressed putative transporter genes followed by confocal live-cell imaging, proliferation assays with knockout and knockdown lines, and protein structure predictions, we identified six proteins that are likely required for ferrous iron transport in *P. falciparum*. *Pf*E140 may be involved in iron uptake into the parasite cytosol across the plasma membrane and *Pf*MRS3 could mediate import of the metal ion into the mitochondrion. *Pf*VIT may transport excess iron from the cytosol into cytoplasmic vesicles, and *Pf*ZIPCO could be implicated in Zn^{2+} and Fe^{2+} export from these organelles, while *Pf*NRAMP and *Pf*CRT are likely responsible for Fe^{2+} efflux from the digestive vacuole. Our results provide new insights into the mechanisms of iron transport in *P. falciparum* and the parasite's response to iron status alterations in the host. *Pf*E140 and *Pf*CRT are particularly promising candidate targets for novel antimalarial drugs, as these are essential to the parasite and lack human orthologs.

INTRODUCTION

Iron is an essential micronutrient for all living organisms and has been associated with virulence of many pathogens. Iron abundance increases the replication of human immunodeficiency virus (HIV) (1) and *Mycobacterium tuberculosis* (2), and promotes biofilm formation in *Pseudomonas aeruginosa* (3). A “fight for iron” has been described between bacteria and the human host in the gastrointestinal tract (4), where the metal skews the composition of the gut microbiome by facilitating the growth of enteropathogenic *Escherichia coli* and *Salmonella* (5). Similarly, cancer cells require more iron compared to healthy cells (6) and higher ferritin levels in individuals diagnosed with COVID-19 were associated with increased disease severity and lethality (7).

Host iron deficiency is known to be protective against severe malaria (8-11) and iron-chelators have cytocidal effects on the human malaria parasite *Plasmodium falciparum* (12). This obligate intracellular parasite depends on free iron for its proliferation and relies entirely on the host to meet its nutrient requirements (13). Furthermore, *P. falciparum* senses environmental fluctuations (14-16) and modulates its virulence in response (16). While iron is crucial for DNA replication and repair, mitochondrial electron transport, and redox regulation, it becomes toxic when in excess, as it is a source of damaging reactive oxygen species (17). Importantly for therapeutic development, the mechanisms of iron acquisition, storage, detoxification, and export in the parasite are different from those in humans due to the absence of transferrin, ferritin, ferroportin, and a functional heme oxygenase in *Plasmodium* (18).

While human blood plasma contains between 10 and 30 µM total iron and an erythrocyte carries approximately 20 mM Fe (19), only 2.5 – 4.7 µM of iron is unbound and bioavailable in uninfected red blood cells, and 1.5 – 1.8 µM in *P. falciparum*-infected ones in the form of ferrous iron, Fe^{2+} (20). An estimated total iron concentration of 500 mM (21) is reached within the parasite’s digestive vacuole (DV), where iron-containing hemoglobin (Hb) is digested and the released heme is detoxified by biocrystallization into hemozoin (22). However, *P. falciparum* cannot access this iron source and is thought to acquire free Fe^{2+} from the host cell (23). Over-elevated concentrations of free iron likely compromise the integrity of the DV membrane and cytosolic iron also needs to be regulated to prevent oxidative stress (18). Iron detoxification in the parasite may be achieved by translocating the metal ion into dynamic intracellular Fe^{2+} stores, which may include acidocalcisomes – cytoplasmic vesicles that contain high concentrations of phosphate, calcium, iron, and zinc (24). In contrast to *Trypanosoma brucei* (24), no transport proteins have yet been experimentally shown to localize to the acidocalcisome membrane in *P. falciparum* (25, 26).

Like the DV, these organelles are thought to be acidified by the plant-like V-ATPase and their low internal pH may fuel secondary active transport processes (22, 27).

P. falciparum encodes approximately 200 transmembrane or membrane-associated transport proteins (channels, pores, carriers, and pumps), many of which are essential for parasite growth and lack orthologs in humans (28). For instance, the vacuolar iron transporter *Pf*VIT (PF3D7_1223700), an ortholog of *Arabidopsis thaliana* VIT1 (expect value (E) = 5 x 10^{-29}, 30.5% identity, 87% coverage, as determined by position-specific iterated BLAST (29)), is a Fe^{2+}/H^{+} exchanger with unknown subcellular localization that likely plays a role in iron detoxification (30-32). The chloroquine resistance transporter *Pf*CRT (PF3D7_0709000) and the natural resistance-associated macrophage protein *Pf*NRAMP (PF3D7_0523800) were both localized to the digestive vacuolar (DV) membrane (33, 34), and have been suggested to export Fe^{2+} into the cytosol in symport with protons. These predicted functions are based on transport assays with *Xenopus* oocytes (35) and homology to the human endosomal Fe^{2+} transporter 2/DMT1 (36), respectively. In *Saccharomyces cerevisiae*, a model organism for eukaryotic iron homeostasis, the mitochondrial carrier protein MRS3 (mitochondrial RNA-splicing protein 3) was shown to ensure Fe^{2+} supply to the mitochondrion (37-39). In *P. falciparum*, the mitochondrion is also the focal point for cellular iron metabolism and contains iron-dependent proteins implicated in the biosynthesis of heme and iron-sulfur clusters, redox reactions, and electron transport (18). It was proposed that its ortholog *Pf*MRS3 (also known as mitoferrin (*Pf*MFRN), PF3D7_0905200, E = 3 x 10^{-14}, 35.1% identity, 26% coverage) mediates Fe^{2+} import into the mitochondrion in *P. falciparum* (40), but its localization had not been experimentally determined prior to this study.

Despite the importance of iron for *P. falciparum* virulence, understanding of the molecular mechanisms of iron sensing, acquisition, utilization, and regulation in the parasite remains limited. The goal of this exploratory study was to dissect how the parasite responds to differences in iron availability in its environment and to identify putative iron transporters as potential new antimalarial drug targets. We investigated growth and gene expression patterns of the laboratory *P. falciparum* strain 3D7 under control (iron-replete), high-iron and low-iron conditions, and in the presence of the iron-regulatory peptide hormone hepcidin. In the human body, hepcidin is produced to reduce the concentration of serum iron when it rises above a certain threshold. The hormone binds specifically to ferroportin on the surface of many cell types including erythrocytes and sterically inhibits the transporter's iron export activity, thereby increasing the concentration of bioavailable intracellular iron and decreasing serum iron levels (41, 42). Here, whole-transcriptome sequencing was used to identify putative iron transport proteins based on differential gene expression patterns between high

vs. low-iron conditions. We then further studied these proteins by assessing their subcellular localization in live parasites, determining the growth rates of knockout or knockdown parasite lines, and analyzing their predicted 3D structures.

RESULTS

Elevated erythrocyte free iron levels promote *P. falciparum* proliferation in vitro

To investigate whether free iron levels in the erythrocyte correlate with parasite replication rates, we established different iron conditions in vitro. The first approach was to culture *P. falciparum* 3D7 parasites in erythrocytes from an individual with high iron status (231 µg/L ferritin, 18.2 g/dL Hb, 51.5% hematocrit), an iron-deficient (43) person (3 µg/L ferritin, 11.4 g/dL Hb, 36.3% hematocrit) and a healthy donor (21 µg/L ferritin, 15.0 g/dL Hb, 42.3% hematocrit). Secondly, infection of red blood cells from other healthy individuals with or without the addition of 0.7 µM hepcidin to the culture medium was compared. This concentration of the iron-regulatory hormone was reported to reduce binding of ferrous iron to ferroportin by 50% in vitro (44), which is expected to increase intracellular Fe^{2+} concentrations.

Relative free iron levels in uninfected erythrocytes were estimated by determining the mean fluorescence intensity (MFI) of the iron-sensitive dye Phen Green SK per cell using flow cytometry. As binding of ferrous iron to the metal-binding moiety causes fluorescence quenching of the fluorophore, a reduction in fluorescence intensity indicates higher free iron levels (45). In erythrocytes from the iron-deficient donor, the Phen Green SK MFI was 43% higher relative to control, confirming the reduced free iron levels (Fig. 1A). The parasite replication rate after one intraerythrocytic developmental cycle (IDC) decreased by 16% (Fig. 1B), the DNA content of late schizonts by 19% (Fig. 1C) and the number of merozoites counted per late schizont by 14% (Fig. 1D). In contrast, bioavailable iron levels of erythrocytes from the donor with high iron status were only slightly increased (without statistical support, two-tailed unpaired *t* tests with Welch's correction for unequal variances and adjusted with the Holm-Šídák method for multiple comparisons, $P = 0.25$) relative to blood with normal iron level (healthy control) – as were the parasite proliferation rate, the DNA content and the merozoite number of mature schizonts (Fig. 1). To further increase intracellular free iron levels, we incubated parasites with 0.7 µM hepcidin during one IDC, resulting in 11% reduced Phen Green SK MFI compared to control (Fig. 1A). Under these conditions, the parasite growth rate increased by 57% (Fig. 1B), the DNA content per schizont by 16% (Fig. 1C), and the number of merozoites produced per schizont by 15% (Fig. 1D).

Taken together, these data show that parasites grown in erythrocytes from an iron-deficient donor displayed significantly reduced growth rates compared to healthy control. Our in vitro results also demonstrate that hepcidin treatment of control erythrocytes elevated intracellular Fe^{2+} concentrations and promoted parasite proliferation. For each condition, independent experiments were carried out on multiple occasions with consistent results.

RNA-sequencing reveals differential expression of putative iron transporters

To identify iron-regulated mechanisms and putative iron transporters in *P. falciparum*, we carried out whole-transcriptome profiling using bulk RNA-sequencing (Fig. 2). *P. falciparum* 3D7 parasites were cultured either using erythrocytes from a donor with high, control (healthy) or low iron status (experiment 1); or with red blood cells from another healthy donor in the presence or absence of 0.7 µM hepcidin (experiment 2). Samples from three biological replicates per condition were harvested at the ring and trophozoite stage (6 – 9 and 26 – 29 hours post invasion, hpi) during the second IDC under the conditions specified.

To exclude the possibility that differences in mRNA abundance were due to divergent progression through the IDC under different nutritional conditions, we assessed the average developmental age of the parasites in each sample based on a statistical maximum likelihood estimation (MLE) method of transcriptional patterns according to Lemieux et al. (46). The general transcriptional patterns of parasites were highly similar at individual time points and consistent across different experimental treatments, corresponding to those of a 3D7 reference strain (47) at approximately 10 hpi and 35 hpi (Fig. 2A). This indicates that differences in mRNA abundance of parasites were not caused by divergent progression through the IDC but by direct effects of the experimental treatments. As the 3D7 strain we used for the experiments had a reduced total IDC length of 44 h instead of 48 h, possibly due to gene deletions that may have occurred during long-term culturing (48, 49), it progresses through the cycle faster than the 3D7 reference strain (47). This may explain why the calculated MLEs of parasite age were higher than the actual values of 6 – 9 hpi and 26 – 29 hpi (Fig. 2A).

Using a threshold of 1.5 for the fold change (FC) in gene expression ($\log_2$ FC of 0.585 or -0.585) yielded twelve significantly upregulated and 175 downregulated genes in ring-stage parasites under high vs. low-iron conditions ($P < 0.05$, exact test for the negative binomial distribution with Benjamini-Hochberg correction (50)). As differences in transporter gene transcription are typically small (51, 52), we examined the 351 upregulated and 770 downregulated genes with a significant expression change and a minimum absolute value of

the $\log_2$ FC of 0.2 for this comparison (Fig. 2B). The full RNA-seq datasets are available in the BioStudies repository (53) under accession number E-MTAB-13411 (https://www.ebi.ac.uk/biostudies/studies/E-MTAB-13411) and differential gene expression test results for individual genes are shown in Supplementary Tables S1 and S2. The highly polymorphic *var*, *stevor*, and *rifin* gene families were excluded from downstream analyses due to their significant sequence diversity between parasites of the same strain during mitotic growth (54, 55). Functional Gene Ontology (GO), Kyoto Encyclopedia of Genes and Genomes (KEGG) and Reactome (REAC) term enrichment analyses of differentially expressed genes (DEGs) were performed using the g:Profiler web server (56).

Under high vs. low-iron conditions at the ring stage (6 – 9 hpi), the GO term for biological process GO:0055085 “transmembrane transport” was 2.8-fold enriched ($P = 0.007$, hypergeometric test) among significantly upregulated parasite genes (Fig. 2C). Using the recently updated *P. falciparum* transporter list (28), all genes with differential expression levels at the ring stage were then screened for transport proteins and all of the five putative iron transporters previously proposed for *Plasmodium* (VIT, ZIPCO, NRAMP, CRT, MRS3/MFRN (18, 57)) were found differentially expressed (Table 1). Other significantly enriched functional terms at the ring stage under high-iron conditions were GO:0009056 “catabolic process”, GO:0020020 “food vacuole”, KEGG:01100 “metabolic pathways”, and GO:0005737 “cytoplasm” (Fig. 2C). Among downregulated genes under high vs. low-iron conditions at the ring stage, KEGG:03440 “homologous recombination”, KEGG:03410 “base excision repair”, GO:0007049 “cell cycle”, and GO:0015630 “microtubule cytoskeleton” were enriched (Fig. 2C). At the more metabolically active trophozoite stage (26 – 29 hpi), processes related to mRNA splicing and protein production were overrepresented in upregulated genes, as indicated by the 2.9-fold enrichment ($P = 0.00006$) of the KEGG:03040 pathway “spliceosome” and the 2.5-fold enrichment ($P < 0.05$) of the GO:0015934 term “large ribosomal subunit” (Fig. 2C).

In contrast, hepcidin treatment resulted in reduced metabolism compared to control conditions, as KEGG:00040 “pentose and glucuronate interconversions”, REAC:R-PFA-71291 “metabolism of amino acids and derivatives”, GO:0005737 “cytoplasm”, and GO:0015934 “large ribosomal subunit” were significantly enriched in downregulated genes during the parasite ring stage at 6 – 9 hpi (Fig. 2E). Among significantly upregulated genes in the presence vs. absence of hepcidin, the terms GO:0070258 “inner membrane pellicle complex” ($P < 0.05$), KEGG:03430 “mismatch repair” ($P = 0.04$), and GO:0015630 “microtubule cytoskeleton” ($P = 0.04$) were enriched at the ring stage. GO:0044409 “entry into host” ($P = 0.00008$) and GO:0052126 “movement in host environment” ($P = 0.0001$)

were overrepresented at the trophozoite stage (Fig. 2E), possibly linked to the observed increase in parasite proliferation (Fig. 1B).

Our RNA-seq data also revealed the differential expression of genes involved in epigenetic, transcriptional, translational, and post-translational regulation. Under high vs. low-iron conditions, histone deacetylation and chromatin organization processes as well as GO:1990904 “ribonucleoprotein complex” were significantly enriched in upregulated genes at the trophozoite stage, and GO:000370 “DNA binding transcription factor activity” in downregulated genes at the ring stage (Fig. 2C). Furthermore, the known iron-regulatory protein *Pf*IRP or aconitate hydratase (58, 59) was upregulated during the ring stage under high vs. low-iron conditions ($\log_2$ FC = +0.49, P = 0.00003) and downregulated in the presence of hepcidin ($\log_2$ FC = -0.27, P = 0.01) as compared to control. Many protein kinases involved in post-translational modifications and endocytosis were also upregulated at 26 – 29 hpi at high vs. low iron levels, as indicated by the enriched terms GO:0043170 “macromolecule metabolic process” and KEGG:04070 “phosphatidylinositol signaling system” (Fig. 2C).

Localization of putative iron transporters in *P. falciparum*

Based on transcriptomic profiles and data from the literature, six proteins with a potential role in iron transport were identified (Table 1 and 2). Of these, *Pf*CRT (60) and *Pf*NRAMP (34) had already been shown to localize to the digestive vacuole (DV) in live parasites (61). The subcellular localization of the other four putative iron transporters (*Pf*MRS3, *Pf*VIT, *Pf*ZIPCO, and *Pf*E140) was then examined by endogenous tagging with GFP and confocal imaging of live parasites under physiological control conditions. At least two cell lines were generated per candidate with consistent results and representative example images are shown in Fig. 3. Diagnostic PCRs confirmed the fusion of *gfp* to the respective gene of interest and the absence of parental DNA at the original locus (Supplementary Fig. S2). Only the *Pf*MRS3 reporter cell line still contained wild-type DNA of the parental parasites even after prolonged WR99210/neomycin selection and limiting dilution cloning (Supplementary Fig. S2), indicating the importance of this mitochondrial transporter for asexual parasite growth during the blood stage.

The GFP-tagged mitochondrial carrier protein *Pf*MRS3 exclusively localized to the mitochondrion, as determined by colocalization with MitoTracker Red (Fig. 3A, Supplementary Video S1). *Pf*VIT-GFP displayed a punctate fluorescence pattern within the cytoplasm (Fig. 3B, Supplementary Video S2), resembling that of *Pf*ZIPCO-GFP (ZIP domain-containing protein, PF3D7_1022300, Fig. 3C, Supplementary Video S3). These

structures did not colocalize with ER Tracker Red in live cells (Fig. 3B, Supplementary Video S2). For both *Pf*VIT-GFP and *Pf*ZIPCO-GFP, the number of cytoplasmic foci increased as the parasites matured from the ring to the late schizont stage (Fig. 3B and C). To test whether these could be acidocalcisomes, we employed LysoTracker Deep Red, commonly used to visualize small acidic organelles in *T. brucei* (24). However, the fluorescent dye only stained the DV in *P. falciparum* (Fig. 3C, Supplementary Video S3) and no acidocalcisome-specific marker is currently available for this parasite.

GFP-tagged *Pf*E140 (PF3D7_0104100), also known as conserved *Plasmodium* membrane protein or CPMP (62), localized to the parasite plasma membrane, as evidenced by the ring-like fluorescence pattern around newly formed merozoites (Fig. 3D, Supplementary Video S4). The fluorescence intensity was very low at the ring and early trophozoite stage compared to schizonts. Based on amino acid sequence similarity ($E = 9 \times 10^{-5}$, 22.5% identity, 66% coverage) to the essential apicoplast transporter *Pf*DER1-2 (29, 63), we also investigated the potential colocalization with the apicoplast marker *Pf*ACP (acyl carrier protein), which could not be detected (Fig. 3D, Supplementary Video S4).

Functional assessment of *Pf*VIT, *Pf*ZIPCO and *Pf*E140

To study the function of the putative transport proteins identified, we used targeted gene disruption (TGD) by selection-linked integration (SLI) to generate the corresponding knockout parasite lines for the putative iron transporters that are non-essential during *P. falciparum* blood stage: *Pf*VIT and *Pf*ZIPCO (Fig. 4A, Supplementary Fig. S2). As GFP was cloned in frame with the truncated version of the respective transporter (the N-terminal 143 amino acids (aa) of 274-aa *Pf*VIT or 117 of the 325 aa of *Pf*ZIPCO), the subcellular localization of the resulting GFP fusion protein was also assessed. *Pf*VIT(1-143)-GFP localized to cytoplasmic structures and *Pf*ZIPCO(1-117)-GFP to the DV and cytoplasmic vesicles (Fig. 4A). Proliferation assays were then performed to determine the importance of the respective transporter for parasite growth. While the *Pf*VIT knockout had no effect on parasite growth under standard conditions, addition of hepcidin reduced the growth rate of the ΔVIT line by 30% (Fig. 4B). Of note, hepcidin generally had a smaller effect after two cycles of incubation (Fig. 4B) than after one cycle compared to the first IDC (Fig. 1B). Unexpectedly, knocking out *Pf*ZIPCO led to a growth rate increase by 42% after two IDCs relative to wild-type 3D7 parasites (Fig. 4B).

For an inducible knockdown of *Pf*E140, which is predicted to be essential (64), a *glmS* ribozyme sequence (65) was introduced upstream of the 3' untranslated region in the pSLI plasmid, allowing for conditional mRNA degradation by adding 2.5 mM glucosamine (GlcN)

to the culture media (Fig. 4C, Supplementary Fig. S2). This led to a 61% decrease in total parasite fluorescence intensity after 36 hours of GlcN treatment (Fig. 4D) without affecting parasite size compared to untreated control (Fig. 4E). GlcN addition also caused a 38% growth rate reduction of the *Pf*E140-GFP-*glmS* line in the absence of hepcidin vs. no significant alteration in the presence of hepcidin relative to standard culture conditions (Fig. 4F). The generation of a *Pf*MRS3-knockdown line was not successful after four independent attempts, supporting the potential essentiality of the gene for asexual growth (64).

Characterization and functional implications of predicted protein structures

We next took advantage of the recent progress in protein structure prediction and generated models of the putative iron transport proteins identified (Table 2) using AlphaFold2 (66, 67) and AlphaFold2-multimer (68). The transmembrane regions of the proteins typically exhibited the highest confidence score, while some other protein portions appeared unstructured (Fig. 5A). Regions that are likely located within a membrane were validated by inspecting the molecular lipophilicity potential of the protein surfaces (Fig. 5B). A clear hydrophobic belt was observed for all proteins and their orientation in the membrane was determined based on that of orthologous proteins. As transport cavities with negatively charged residues are a hallmark of heavy metal ion transporters, we analyzed the distribution of charge on the surface of the proteins and looked for negatively charged regions to assess the capacity to bind cations like Fe^{2+} (Fig. 5C). To gain further insights into the functions of the proteins identified, we also compared the predicted structures with those of well-characterized putative orthologs from *S. cerevisiae*, *Eucalyptus grandis, Bordetella bronchiseptica* and *Staphylococcus capitis* (Table 2, Supplementary Fig. S3 and S4).

The outer surface of *Pf*MRS3 (transport classification (TC): 2.A.29, mitochondrial carrier family) is positively charged (Fig. 5C) and there is a clear negatively charged patch in the putative binding pocket facing the mitochondrial intermembrane space. We compared the predicted *Pf*MRS3 structure with that of *S. cerevisiae* MRS3, which is known to import ferrous iron into the mitochondrial matrix across the inner membrane (37-39). The predicted structures of *Pf*MRS3 and *S. cerevisiae* MRS3 were superimposed with an average root mean square deviation of Cα atoms (Cα RMSD) of the 205 matched residues of 2.3 Å (Supplementary Fig. S3A and S4A). The conserved histidine residues His^{48} and His^{105} that were required for Fe^{2+} transport by *S. cerevisiae* MRS3 in reconstituted liposomes (37) are also present in *Pf*MRS3 and the three functionally relevant histidine residues identified in yeast are in a similar functional context in both structures (Supplementary Fig. S3A and S4A). This suggests that MRS3 may elicit similar molecular functions in *S. cerevisiae* and *P. falciparum.*

*Pf*VIT is highly similar to VIT1 from *E. grandis* (E = 7 x 10^{-27}, 30.3% identity, 84% coverage), for which an experimental structure is available (PDB 6IU4). The plant protein crystallized as a homodimer (69), and the same oligomeric state was suggested for the vacuolar iron transporter family (TC: 2.A.89) protein in *P. falciparum* (31). A *Pf*VIT monomer also has five transmembrane domains and comprises a negatively charged region facing the cytosol that may enable cation transport (Fig. 5C). In agreement with this, one Fe^{2+} ion and two Zn^{2+} ions were bound by a strongly charged region on the cytosolic side of the *E. grandis* VIT1 monomer (69) and a highly similar putative binding pocket is present in the parasite protein (Supplementary Fig. S4B). In the structural alignment, 219 of the 227 residues of the experimental *Eg*VIT1$^{23-249}$ structure are within 5 Å of the predicted structure of *Pf*VIT with an average Cα RMSD of 1.9 Å and the key residues in the metal-binding domain (Glu^{102}, Glu^{105}, Glu^{113}, Glu^{116}, using *Eg*VIT1$^{23-249}$ numbering) are placed in a similar molecular context in the predicted structure of *Pf*VIT (Supplementary Fig. S3B and S4B). The residues in the transmembrane domain that are in the vicinity of the Co^{2+} ion in the *Eg*VIT1$^{23-249}$ structure (Met^{80} and Asp^{43}) are also conserved (Supplementary Fig. S3B). These results strongly suggest that *Pf*VIT functions similarly to *Eg*VIT1.

*Pf*ZIPCO contains seven transmembrane domains and was modeled as a homodimer (Fig. 5A), as it is part of the zinc (Zn^{2+})-iron (Fe^{2+}) permease (ZIP) family (TC: 2.A.5), whose members usually function as homo- or heterodimers (70). The negatively charged patch in each binding pocket facing the vesicle lumen (Fig. 5C) may be involved in cation transport to the cytosolic side. In an overlay of the *Pf*ZIPCO model with the cryo-EM structure (PDB 8GHT) of a ZIP transporter from *B. bronchiseptica* in the presence of either Zn^{2+} or Cd^{2+} ions (71), the average Cα RMSD of 140 sequence-aligned residues was 2.0 Å (Supplementary Fig. S3C and S4C). Several key residues of the metal binding site M1 of *Bb*ZIP (Met^{99}, His^{177}, Glu^{181}, Glu^{211}) were also found in *Pf*ZIPCO, whereas others (Asn^{178}, Gln^{207}, Asp^{208}, Glu^{240}) were different (Supplementary Fig. S3C), possibly resulting in divergent substrate specificity.

Like *Pf*CRT (TC 2.A.7, drug/metabolite exporter family), for which a recent cryo-EM structure (PDB: 6UKJ) is available (72), the predicted structure of *Pf*NRAMP (TC: 2.A.55, metal ion (Mn^{2+}-iron) transporter family) contains ten transmembrane domains (Fig. 5A) and a negatively charged region within its binding pocket facing the digestive vacuolar lumen (Fig. 5C). This is consistent with binding of cations such as Fe^{2+}. The *Pf*NRAMP model was superimposed on the solved crystal structure of *S. capitis* NRAMP/DMT (PDB code: 5M95, E = 1 x 10^{-32}, 26.3% identity, 60% coverage), which was shown to bind Mn^{2+}, Fe^{2+}, Co^{2+}, Ni^{2+},

Cd^{2+} and Pb^{2+} (73). In the overlay, the average Cα RMSD of the 349 matched residues was 1.6 Å and the negatively charged cavity of *Pf*NRAMP was in close proximity to the Mn^{2+} ion bound to *S. capitis* NRAMP (Supplementary Fig. S3D and Supplementary Fig. S4D). Two of the four key residues required for ion coordination in the binding pocket of the bacterial protein (Asn^{52} and Asp^{49}) are present in *Pf*NRAMP, while the two other residues (Met^{226} and Ala^{223}) are changed to serine (73). *Pf*NRAMP is thus likely to perform cation transport from the DV into the cytosol.

*Pf*E140 is predicted to be anchored in the parasite plasma membrane by a bundle of five transmembrane domains (74) and forms a coiled coil with a hydrophilic region that displays negatively charged patches exposed to the extracellular side (Fig. 5A and B). No human orthologs could be identified for this highly conserved *Plasmodium* protein (29). As there is no obvious channel or cavity in the transmembrane region of the *Pf*E140 monomer (Fig. 5B and C), the helical bundles may form a dimer to enable ion transport. However, we were not able to obtain a *Pf*E140 dimer model with AlphaFold2-multimer due to its sequence length. To predict functional residues based on the amino acid sequence and the AlphaFold2 structure of *Pf*E140, we used DeepFRI graph convolutional network (75), which has significant denoising capability and can reliably assign GO terms to residues in the protein. In particular, the terms GO:0022857 “transmembrane transporter activity” (DeepFRI gradCAM score 0.94), GO:0015075 “monoatomic ion transmembrane transporter activity“ (score 0.78), and GO:0046873 “metal ion transmembrane transporter activity” (score 0.67) were assigned to a putative transmembrane region of *Pf*E140 with high confidence (Supplementary Fig. S5). We thus speculate that the protein is a transporter of metal ions.

DISCUSSION

Here, we studied the role of iron in growth and transcription of *P. falciparum* using blood from individuals of different iron status and by adding hepcidin as an iron-regulatory hormone and ferroportin inhibitor. Overall, our data demonstrate the importance of Fe^{2+} in parasite replication and development and highlight areas for further study. We showed that in vitro growth rates of *P. falciparum* 3D7 and the number of merozoites formed per schizont were reduced within erythrocytes that contain lower concentrations of free iron, while culturing in blood from an individual with high iron status did not lead to a significant increase in free iron levels within erythrocytes or in parasite growth relative to control (Fig. 1). Consistent with this, reduced propagation of *P. falciparum* 3D7, Dd2, and FCR3-FMG was reported when erythrocyte samples from iron-deficient individuals used for parasite culture (10, 76). This effect was eliminated after these donors were iron-supplemented, while supplementation of healthy (iron-replete) donors did not significantly promote parasite

growth (10). The strong increase in parasite replication in the presence of hepcidin relative to control conditions (Fig. 1B) may have been due to enhanced invasion efficiency in addition to the increased number of merozoites formed (Fig. 1D). Previous reports also indicated that higher hepcidin levels in blood samples were associated with elevated *P. falciparum* growth rates in vitro (76) and severe malaria in vivo (77).

To identify putative iron transporters and iron-regulated processes, we carried out RNA-sequencing analyses of *P. falciparum* during the ring (6 – 9 hpi) and trophozoite (26 – 29 hpi) stages cultured under the different iron conditions described above. A higher number of biological processes and pathways were significantly enriched among DEGs when erythrocytes from donors with different iron status were used for parasite culture (Fig. 2C) compared to red blood cells from the same healthy donor in the presence vs. absence of hepcidin (total of 28 vs. 13 functional terms, Fig. 2E). This may reflect greater differences in the culture conditions; for instance, blood from the donor with high ferritin and Hb levels may have also contained more glucose or copper (78, 79), potentially explaining the more diverse physiological response of the parasite. Including erythrocyte samples from more individuals in the growth experiments and RNA-seq analysis would have provided further insights, however, the provision of sufficient blood from iron-deficient donors is limited by ethical constraints.

The availability of additional nutrients likely resulted in increased endocytosis and digestion of host cell contents in the DV of the parasite, leading to enhanced metabolism, mRNA splicing, and protein production. Interestingly, the terms KEGG:01100 “metabolic pathways” and GO:0005737 “cytoplasm” were also found to be enriched in upregulated parasite genes in children with high vs. low parasitemia (80, 81). RNA binding and mRNA splicing processes were previously reported to be overrepresented in upregulated genes in severe malaria linked to high parasite density (80-82). Hence, an increase in overall parasite fitness under high vs. low-iron conditions may explain the increase in parasite multiplication (Fig. 1B) and could be associated with higher parasitemia and disease severity. Consistent with the observed upregulation of transmembrane transporters at the parasite ring stage (6 – 9 hpi) under high vs. low-iron conditions, Mancio-Silva et al. found that the functional term “ion transporter activity” was enriched in *Plasmodium berghei* genes that were downregulated under caloric restriction at 6 and 10 hpi (16). Thus, transmembrane transporter genes may need to be transcribed at the beginning of the IDC to ensure that the appropriate level of transport proteins is available for nutrient acquisition and metabolite efflux during the subsequent metabolically active trophozoite and schizont stages.

Hepcidin plays a central role in mammalian iron homeostasis and reduces serum iron concentrations (83). It is also known that hepcidin levels are elevated in *P. falciparum*-infected individuals, especially those with high parasitemia (77, 84), and that malaria causes iron deficiency (77). The transcription profile of parasites treated with hepcidin showed similarities to those cultured in erythrocytes from the iron-deficient donor compared to standard conditions in terms of downregulated catabolic and translation processes as well as transport protein regulation (Fig. 2, Table 1). The upregulation of genes involved in merozoite motility (*Pf*MTIP, *Pf*GAP45, and various inner membrane complex proteins) and host cell entry (such as *Pf*AMA1, *Pf*MSP3, *Pf*MSP7, and *Pf*EBA181) when hepcidin was present (Fig. 2) may suggest an improved ability of the released merozoites to invade erythrocytes. Thus, the addition of the peptide hormone to the culture media may be a signal for the parasite to reduce metabolic processes and to increase its replication and invasion efficiency.

In addition to roles in parasite proliferation and development, different levels of bioavailable iron may induce regulatory processes at various levels. Under high-iron conditions, the observed upregulation of histone deacetylation (Fig. 2C) may lead to the condensation and thus deactivation of certain chromatin regions (85). Similarly, iron-mediated regulation of mRNA translation by iron-regulatory proteins has been described in yeast, trypanosomes and mammals (86-88). The binding sites and target genes of the differentially expressed transcription factors and of *Pf*IRP remain to be identified in *P. falciparum*. Moreover, protein phosphorylation may play a role in iron-dependent regulatory mechanisms. As a serine/threonine kinase (KIN) serves as a nutrient sensor in *P. berghei*, driving a fast response that leads to increased parasite multiplication and virulence (16), a similar kinase may sense iron and lead to increased replication in *P. falciparum*.

Based on our RNA-sequencing results and data from the literature (Fig. 2 and Table 1), we identified six proteins that are likely involved in *P. falciparum* iron transport (Table 2 and Figure 6) and analyzed their subcellular localization (Fig. 3), their importance for growth (Fig. 4), and their predicted structures (Fig. 5). *Pf*MRS3 transcription was upregulated at the ring stage under high vs. low-iron conditions ($\log_2$ FC = 0.33, P = 0.002, Fig. 2B), and fluorescence of the GFP-tagged protein was exclusively detected at the mitochondrion (Fig. 3A). As a disruption of the gene was reported to fail (64), we were not able to generate a knockdown line after four independent attempts, and parental DNA of the original gene locus was still present in the GFP reporter line (Supplementary Fig. S2), *Pf*MRS3 is likely essential for asexual growth like PBANKA_041620 (E = 1×10^{-69}, 71.4% identity, 25% coverage) in *P. berghei* (89). The orthologous mitochondrial iron transporter (*Tg*MIT, TGME49_277090, E =

494 7 x 10^{-19}, 26.0% identity, 28% coverage) also localized to the mitochondrion in *T. gondii* and
495 was upregulated at the protein level upon iron overload due to a *Tg*VIT knock out in the
496 related apicomplexan parasite (90). In line with our structural analyses (Fig. 5,
497 Supplementary Fig. S3A and S4A), *Pf*MRS3 may thus import ferrous iron into the
498 mitochondrion – the main iron user of the cell – and thereby reduce the cytosolic Fe^{2+}
499 concentration (Fig. 6) as a means of detoxification, as previously described in yeast (91).
500 The protein's substrate specificity as well as iron binding and transport activity remain to be
501 confirmed experimentally.
502
503 *Pf*VIT was suggested to be involved in iron detoxification in *Plasmodium* (30) and its
504 expression was upregulated under high vs. low-iron conditions ($\log_2$ FC = +0.29, P = 0.02,
505 Fig. 2B). The fluorescence pattern of *Pf*VIT-GFP in live cells (Fig. 3B) was consistent with
506 cytoplasmic vesicles that may be acidocalcisomes, as described for *T. brucei* VIT1 (24). An
507 increase in the number of fluorescent punctate structures during parasite development (Fig.
508 3B) was also observed for VIT in *Toxoplasma gondii* (90). *Pf*VIT shares 47.0% identity with
509 *Tg*VIT (E = 8 x 10^{-84}, 95% coverage) and 36.9% identity with *Tb*VIT1 (E = 9 x 10^{-39}, 98%
510 coverage). In contrast, *P. berghei* VIT (PBANKA_143860, E = 3 x 10^{-160}, 79.3% identity, 98%
511 coverage) was shown to localize to the ER in indirect immunofluorescence assays (30). This
512 may be explained by differences between species or variation in methodology such as
513 fixation, permeabilization, and immunolabeling techniques as opposed to live-cell imaging
514 (92-94). While not essential during asexual blood stages (64), a knockout of VIT resulted in
515 reduced liver stage development in *P. berghei* (30) and increased sensitivity to high iron
516 levels in both *P. berghei* (30) and *T. gondii* (90). Similarly, growth of the ΔVIT *P. falciparum*
517 line was not affected under standard conditions, whereas the addition of hepcidin – which
518 increases free intracellular iron levels (Fig. 1A) – compromised parasite proliferation in our
519 study (Fig. 4B). The high similarity of the putative Fe^{2+}-binding pocket in the predicted *Pf*VIT
520 structure with that of the experimentally characterized *Eg*VIT1 (69) and the conservation of
521 key residues for metal ion binding indicate that *Pf*VIT is capable of Fe^{2+} translocation (Fig. 5,
522 Supplementary Fig. S3B and S4B). Thus, the transporter may contribute to iron
523 detoxification by Fe^{2+} sequestration into cytoplasmic vesicles (Fig. 6) and ΔVIT parasites
524 may be more sensitive to elevated intracellular iron concentrations due to impaired removal
525 of excess iron from the cytosol.
526
527 *Pb*ZIPCO (PBANKA_050650) was localized to the parasite plasma membrane (PPM) in *P.*
528 *berghei* sporozoites in indirect immunofluorescence assays and suggested to transport both
529 Zn^{2+} and Fe^{2+} (95). In *P. falciparum*, however, the GFP fusion protein caused a punctate
530 fluorescence pattern in the cytoplasm of live cells (Fig. 3C), similar to that of *Pf*VIT-GFP (Fig.

3B). While the *Pf*ZIPCO knockout caused a growth increase under standard conditions (Fig. 4B), ΔZIPCO *P. berghei* parasites displayed normal blood stage development and impaired sporozoite infectivity in mice (95). Interestingly, the ortholog TGME49_225530 in *T. gondii* is also dispensable with a phenotype score of −2.94 (values below -1.5 are considered non-essential (96)). Hence, Fe^{2+} efflux via *Pf*ZIPCO from cytoplasmic vesicles (potentially acidocalcisomes) may be dispensable in *P. falciparum* under iron-replete conditions during the blood stage, and the production of the transporter may come at a fitness cost, while sporozoites may rely on its activity in low-iron environments. As the transcription of *Pf*ZIPCO was upregulated at low vs. control iron levels ($\log_2$ FC = 0.55, P = 0.04, Table 1) and in response to hepcidin treatment ($\log_2$ FC = 0.63, P = 0.006, Fig. 2D, Table 1), the transport protein may release Zn^{2+} and Fe^{2+} ions from intracellular stores, in this case cytoplasmic vesicles (Fig. 6), in case of scarcity, thereby increasing cytosolic ion levels like other ZIP transporters (57). While our analyses of the predicted structure and the structural alignment with *Bb*ZIP indicate that *Pf*ZIPCO likely has the capacity to bind and transport cations like Zn^{2+} or Fe^{2+} (Fig. 5, Supplementary Fig. S3C and S4C), its substrate specificity can only be conclusively established by characterizing the purified protein. Liposomal assays with the putative zinc transporter *Pf*ZIP1 (PF3D7_0609100, 24.5% identity with *Pf*ZIPCO, E = 1×10^{-19}, 78% coverage), which localized to the plasma membrane in schizonts, demonstrated that this ZIP transporter preferentially binds Zn^{2+} over Fe^{2+} (97). Interestingly, the preference was abolished if the histidine-rich loop at the C-terminus of *Pf*ZIP1, which is not present in *Pf*ZIPCO, was truncated. As mRNA levels of *Pf*ZIP1 were enhanced at low cytosolic Zn^{2+} levels (97) but not differentially regulated under various iron conditions (Supplementary Tables S1 and S2), it may play a role in zinc rather than iron homeostasis under physiological conditions.

As the highest intracellular iron concentration in *P. falciparum* is reached within the DV (21, 98), the free form of the metal may need to be exported from this compartment under high-iron conditions to prevent damage to the DV membrane (Fig. 6). This function may be performed by *Pf*CRT (35) and / or *Pf*NRAMP (36), which were both upregulated under high vs. low-iron conditions in our RNA-seq analysis ($\log_2$ FC = 0.26, P = 0.007 and $\log_2$ FC = 0.28, P = 0.003, respectively, Fig. 2B, Table 1) and are essential in asexual parasites (33, 34, 64). The predicted structure of *Pf*NRAMP (Fig. 5) likely reflects the state that is open towards the cytosol as in the crystal structure of NRAMP from *Deinococcus radiodurans* (99). While a negatively charged cavity inside the protein is clearly visible in the *Pf*NRAMP model, the proposed outward-facing permeation pathway for metal ions is likely occluded in this conformation (Fig. 5C). It is conceivable that Fe^{2+} ions permeate through this pathway from the DV lumen and bind to the charged cavity like the Mn^{2+} ion to *S. capitis*

NRAMP/DMT (Supplementary Fig. S4D). *Pf*NRAMP might function similarly to its ortholog in *D. radiodurans*, which was shown to mediate pH-dependent transport of Fe^{2+} and Mn^{2+} in symport with H^+ using uptake assays in *E. coli*, HEK293T cells, and proteoliposomes (99, 100).

Expression of the surface protein *Pf*E140 was upregulated when iron levels were low compared to standard conditions ($\log_2$ FC = 0.65, P = 0.0006, Table 1) and the GFP fusion protein localized to the PPM only, as evidenced by the fluorescent edges of free merozoites (Fig. 3D). This observation is consistent with the fact that the extracellular portions of this protein are highly polymorphic due to their exposure to the immune system at the sporozoite stage (74). Interestingly, vaccines targeting *Py*E140 in *Plasmodium yoelii* were reported to induce up to 100% sterile protection mediated by antibodies in mice (101). The reduced parasite replication rate upon its conditional knockdown (Fig. 4D) demonstrates the importance of *Pf*E140 for parasite growth. Its predicted essential nature (64), in addition to the absence of orthologs in humans, make it an excellent drug target candidate. While our *P. falciparum* gene expression data (Fig. 2B and D) point towards a role of *Pf*E140 in iron homeostasis, its precise function is still unclear and it remains to be clarified whether the large coiled-coil domain exposed to the extracellular space (Fig. 5) can mediate dimerization upon substrate binding. Given our experimental results and the functional annotations (Fig. 5C, Supplementary Fig. S5), we hypothesize that *Pf*E140 is a plasma membrane transporter for inorganic cations such as metal ions.

In conclusion, this is the first study to investigate *P. falciparum* transcriptomics under different iron conditions and to determine the subcellular localization of the putative iron transport proteins *Pf*MRS3, *Pf*VIT, *Pf*ZIPCO and *Pf*E140. These results improve our understanding of how the human malaria parasite reacts to alterations in the iron status of its host and provide new insights into the mechanisms of iron transport in *P. falciparum*. We propose a new model for iron homeostasis in the *P. falciparum*-infected erythrocyte (Fig. 6) with a series of six organelle-specific iron transport proteins that were identified based on differential gene expression patterns, subcellular localization, proliferation assays, protein structure predictions, and the assessment of putative binding sites using structural alignments with well-characterized proteins. Formal demonstration of the substrate specificity and activity of the transporters will require transport assays with purified proteins in future studies.

Further functional characterization of the parasite transporters identified in this exploratory research is expected to facilitate the development of new therapeutic strategies against

malaria. Due to the absence of human orthologs of the essential proteins *Pf*E140 and *Pf*CRT, which both likely increase iron transport into the parasite cytosol, these provide candidate targets for urgently needed antimalarial drugs. In addition, dissecting how *P. falciparum* senses changes in micronutrient availability in its environment and how it modulates its virulence accordingly is an area of considerable interest for future investigation, as iron is an essential regulatory signal for virulence factors in many pathogens.

MATERIALS AND METHODS

P. falciparum culture and proliferation assays

The *P. falciparum* strain 3D7 was cultured according to modified standard procedures (102) at 5% hematocrit using human 0 Rh+ erythrocytes from the University Medical Center Hamburg-Eppendorf (UKE), Germany, at 1% O_2, 5% CO_2 and 94% N_2. RPMI 1640 medium was supplemented with 0.5% (w/v) AlbuMAX II, 20 µg/mL gentamicin and 100 µM hypoxanthine (Thermo Fisher Scientific). Mature schizonts were obtained by treating schizonts at 40 hpi with 1 mM compound 2 (4-[7-[(dimethylamino)methyl]-2-(4-fluorphenyl)imidazo[1,2-α]pyridine-3-yl]pyrimidin-2-amine, LifeArc) for 8 h. To count the number of merozoites per mature schizont, Giemsa-stained blood smears were analyzed by light microscopy. Only single-infected cells with one digestive vacuole were taken into account.

To assess parasite proliferation over six days, a previously described assay based on flow cytometry was employed (103). Parasites were synchronized to a 3-h age window by isolating late schizonts from a 60% Percoll (GE Healthcare, Life Sciences) gradient and culturing these for 3 h with fresh erythrocytes (104), followed by controlled elimination of advanced parasite stages using 5% (w/v) D-sorbitol (Carl Roth) for 10 min at 37°C (105). The growth assay was started at 0.1% parasitemia using the resulting ring-stage parasites at 0 – 3 hpi. The parasitemia was determined at the trophozoite stage every two days by flow cytometry and culture media with the respective supplements were exchanged daily.

Flow cytometry

To determine parasitemia, 20 µL of resuspended parasite culture was added to 80 µL culture medium and stained with 5 µg/mL SYBR Green I (Thermo Fisher Scientific) and 4.5 µg/mL dihydroethidium (DHE, Sigma) in the dark for 20 min at room temperature. Stained cells were washed with PBS three times and analyzed with an ACEA NovoCyte flow cytometer and NovoExpress Software (version 1.6.1, Agilent). Forward and side scatter gating was

used to identify erythrocytes and SYBR Green I fluorescence intensity to determine the number of parasitized cells per 100,000 events recorded for each sample. For Phen Green SK measurements, uninfected erythrocytes were washed with PBS and incubated with 10 µM Phen Green SK in PBS at 37°C for 60 min. DHE at 4.5 µg/mL was added during the last 20 min of incubation. After three washes with PBS, the cells were analyzed as described above.

Cloning of DNA constructs

For generating the GFP reporter lines, a homologous region of approximately 800 bp at the 3' end of the respective gene was amplified without the stop codon from 3D7 gDNA using Phusion high fidelity DNA polymerase (NEB). A homology region of about 400 bp at the 5' end of the respective gene was used for targeted gene disruption. The fragments were then inserted into pSLI-GFP (106) using Not*I* and Avr*II* restriction sites. For *glmS* constructs, pSLI-GFP-*glmS* (107) was used as a vector instead. All oligonucleotides and plasmids used in this study are listed in Supplementary Table S3.

Transfection of *P. falciparum*

As described previously (108), parasites at the late schizont stage were purified using 60% Percoll (104) and electroporated with 50 µg DNA of the respective plasmid in a 0.2-cm gap cuvette (Bio-Rad Laboratories) using Amaxa Nucleofector 2b (Lonza, Switzerland). Either 4 nM WR99210 (Jacobus Pharmaceuticals) or 2 µg/mL blasticidin S (Life Technologies, USA) was used for selecting transfectants. For the selection of parasites that were genomically modified using the SLI system (106), 400 µg/mL G418 (ThermoFisher, USA) was added to the culture medium once the parasitemia reached 5%. After the selection of modified parasites, genomic DNA was isolated with the QIAamp DNA Mini Kit (Qiagen) and diagnostic tests for correct integration into the genome were performed as specified earlier (106).

Confocal live-cell microscopy

Erythrocytes infected with parasites at different stages at 3 – 6% parasitemia were incubated in culture medium with 20 nM MitoTracker Red, 200 nM ER Tracker Red or 100 nM LysoTracker Deep Red (if applicable) at 37°C for 20 min. Then, 200 nM Hoechst-33342 (Invitrogen) was added for 10 min prior to washing the cells with Ringer's solution (122.5 mM NaCl, 5.4 mM KCl, 1.2 mM $CaCl_2$, 0.8 mM $MgCl_2$, 11 mM D-glucose, 25 mM HEPES, 1 mM NaH_2PO_4, pH 7.4) prewarmed to 37°C and seeding on a chambered No. 1.5 polymer cover slip (Ibidi GmbH). After 5 min, unbound erythrocytes were removed by washing with Ringer's solution and the sample was placed into an incubation chamber that maintained the

microscope work area including the objective at 37°C. Images and videos were acquired using an SP8 confocal microscope system with a 63x oil-corrected lens (C-Apochromat, numerical aperture, NA = 1.4) and Lightning deconvolution software (Leica), and processed using ImageJ version 2.9.0/1.53t (109). If fluorescence intensities were to be quantified, no averaging or deconvolution software was applied.

glmS-based knockdown

For *glmS*-based knockdown induction (65), highly synchronous parasites at early ring stage were cultured with or without supplementation with 2.5 mM glucosamine (GlcN, Sigma-Aldrich). The knockdown was quantified by confocal live-cell microscopy using schizonts 36 h post GlcN treatment initiation. Images of parasites of similar size were acquired with the same settings and background-corrected fluorescence intensities (integrated density) as well as the size of the region of interest were determined using ImageJ version 2.9.0/1.53t (109), and the data visualized using Graph Pad Prism version 9.4.1.

Sample collection for RNA extraction and RNA sequencing

Parasites were synchronized within a 3-h window after invasion of erythrocytes from the respective donor as described above. Samples for RNA-sequencing were prepared in triplicate for each condition and time point, i.e. three separate parasite cultures each were grown in parallel for a total of at least two weeks. During the second IDC, two 10-mL dishes each were harvested for parasites at the ring stage (6 – 9 hpi) and one 10-mL dish each for trophozoites (26 – 29 hpi). Samples were collected by centrifuging the culture for 5 min at 800 g and 37°C and dissolving the erythrocyte pellet using 5 mL TRIzol prewarmed to 37°C, followed by immediate transfer to -80°C for storage. The parasitemia was 0.3% at the start of the experiments with high, control and low-iron donor blood and 2 – 3% at the time of harvest. Parasite cultures treated with 0.7 µM hepcidin (Bachem) had a starting parasitemia of 0.6% and untreated cultures 1% to reach a parasitemia of 4 – 5% during the second cycle. For each experiment, the parasitemia was kept consistent at the point of harvest as high parasite densities can affect transcription (15).

For RNA extraction, the samples frozen in TRIzol were thawed, mixed thoroughly with 0.1 volume cold chloroform, and incubated at room temperature for 3 min. Following centrifugation at 20,000 g and 4°C for 30 min, the supernatants were transferred to fresh vials and combined with 70% ethanol of equal volume. RNA was purified using the RNeasy MinElute Kit (Qiagen) by on-column DNase I digest for 30 min and elution with 14 µL water. The GLOBINclear Human Kit (ThermoFisher Scientific) was then employed to deplete human globin mRNA in all samples. The Qubit RNA HS Assay Kit and Qubit 3.0 fluorometer

(ThermoFisher Scientific) were used for RNA quantification. Upon arrival at the EMBL Genomics Core Facility (GeneCore Heidelberg, Germany), the RNA quality of each sample was evaluated using the RNA 6000 Nano kit and Bioanalyzer 2100 (Agilent). The median RNA integrity number (RIN) of all samples was 7.30 (IQR: 6.85 – 8.15, Supplementary Fig. S1). Individually barcoded strand-specific libraries for mRNA sequencing were prepared from total RNA samples of high quality (approximately 150 ng per sample) using the NEBNext® RNA Ultra II Directional RNA Library Prep Kit (New England Biolabs) for 12 PCR cycles on the liquid handler Biomek i7 (Beckman Coulter GmbH) at GeneCore. Libraries that passed quality control were pooled in equimolar amounts, and a 2 pM solution of this pool was sequenced unidirectionally on a NextSeq® 500 System (Illumina) at GeneCore, resulting in about 500 million reads of 85 bases each.

RNA sequencing read mapping and data analysis

Following successful initial quality control of the RNA-sequencing reads with FastQC version 0.11.8 (110), sequencing adapters were trimmed using Cutadapt version 2.10 (111). A genome index was generated using the FASTA sequence file of the *P. falciparum* 3D7 genome release 46 (PlasmoDB-46_Pfalciparum3D7_Genome.fasta) and the GFF3 annotation file (PlasmoDB-46_Pfalciparum3D7.gff), both obtained from PlasmoDB (112), with STAR version 2.7.5c (113). The same R package was used to align reads to the genome with a maximum of three allowed mismatches (--outFilterMismatchNmax 3). To consolidate the results obtained with FastQC and STAR alignments, a single report file was created using MultiQC version 1.9 (114).

The mapped reads were then summarized in Sequence Alignment/Map (SAM) format using featureCounts (115) from the R package Rsubread version 2.2.1 (116). For counting mapped reads per gene using featureCounts, fragments with a minimum length of 50 bases were considered (minFragLength = 50). Therefore, gene IDs and lengths of transcripts were extracted from PlasmoDB-46_Pfalciparum3D7_AnnotatedTranscripts.fasta with SAMtools faidx version 1.10.2 (117). The R package edgeR 3.30.3 (118) was used to compute RPKM values (reads per kilobase per million mapped reads) and for differential gene expression analysis. Gene annotations were retrieved from PlasmoDB (112) and PhenoPlasm (119). The results of these analyses were visualized with volcano plots using the R package Enhanced Volcano version 1.15.0 (120). The raw and processed data (FASTA files, RPKM values and results of the differential gene expression analysis) can be accessed at https://www.ebi.ac.uk/biostudies/studies/E-MTAB-13411.

The highly polymorphic *var*, *stevor*, and *rifin* gene families were excluded from downstream analyses due to their great sequence diversity between parasites of the same strain during mitotic growth (54, 55). Genes that were significantly regulated (defined as $P < 0.05$ according to the exact test for the negative binomial distribution with Benjamini-Hochberg correction (50) and an absolute value of $\log_2 FC \geq 0.2$) were subjected to functional enrichment analysis with g:Profiler (https://biit.cs.ut.ee/gprofiler/gost (56), accessed on August 17, 2022). The resulting GO, KEGG and REAC terms were summarized using REVIGO (http://revigo.irb.hr/) with the similarity value set to 0.5 (121) and visualized as in Thomson-Luque et al. (81) using the scientific color map "roma" (122). To estimate parasite age, an algorithm developed by Avi Feller and Jacob Lemieux (46) was adapted to use expression data from Broadbent et al. (47) with the time points 6, 14, 20, 24, 28, 32, 36, 40, 44, and 48 hpi as reference. The code and data used were deposited to Zenodo with the record ID 7996302 (https://zenodo.org/record/7996302).

Protein structure prediction

Structure predictions for monomeric proteins were obtained from AlphaFold Protein Structure Database version 3 (66, 67) and homodimeric proteins were predicted using AlphaFold2-multimer version 2.2.2, database version 2.2.0 (68) deployed at the EMBL Hamburg computer cluster. Molecular visualization was performed with UCSF ChimeraX version 1.3 (123). UCSF Chimera MatchMaker and Match → Align tools with default settings were used for structural comparison of the predicted structures of *P. falciparum* proteins with putative orthologs and sequence alignments were generated using the Match → Align tool (124). The DeepFRI server (https://beta.deepfri.flatironinstitute.org) was used to identify possible functional residues with the DeepFRI graph convolutional network (75).

REFERENCES

1. Drakesmith H, Prentice A. Viral infection and iron metabolism. Nat Rev Microbiol. 2008;6(7):541-52.
2. Zhang L, Hendrickson RC, Meikle V, Lefkowitz EJ, Ioerger TR, Niederweis M. Comprehensive analysis of iron utilization by *Mycobacterium tuberculosis*. PLoS Pathog. 2020;16(2):e1008337.
3. Kang D, Kirienko NV. Interdependence between iron acquisition and biofilm formation in *Pseudomonas aeruginosa*. J Microbiol. 2018;56(7):449-57.
4. Sousa Gerós A, Simmons A, Drakesmith H, Aulicino A, Frost JN. The battle for iron in enteric infections. Immunology. 2020;161(3):186-99.
5. Paganini D, Zimmermann MB. The effects of iron fortification and supplementation on the gut microbiome and diarrhea in infants and children: a review. Am J Clin Nutr. 2017;106(Suppl 6):1688s-93s.
6. Brown RAM, Richardson KL, Kabir TD, Trinder D, Ganss R, Leedman PJ. Altered iron metabolism and impact in cancer biology, metastasis, and immunology. Front Oncol. 2020;10:476.
7. Taneri PE, Gómez-Ochoa SA, Llanaj E, Raguindin PF, Rojas LZ, Roa-Díaz ZM, et al. Anemia and iron metabolism in COVID-19: a systematic review and meta-analysis. Eur J Epidemiol. 2020;35(8):763-73.

8. Nyakeriga AM, Troye-Blomberg M, Dorfman JR, Alexander ND, Bäck R, Kortok M, et al. Iron deficiency and malaria among children living on the coast of Kenya. J Infect Dis. 2004;190(3):439-47.
9. Gwamaka M, Kurtis JD, Sorensen BE, Holte S, Morrison R, Mutabingwa TK, et al. Iron deficiency protects against severe *Plasmodium falciparum* malaria and death in young children. Clin Infect Dis. 2012;54(8):1137-44.
10. Clark MA, Goheen MM, Fulford A, Prentice AM, Elnagheeb MA, Patel J, et al. Host iron status and iron supplementation mediate susceptibility to erythrocytic stage Plasmodium falciparum. Nature Communications. 2014;5:4446.
11. Brabin L, Roberts SA, Tinto H, Gies S, Diallo S, Brabin B. Iron status of Burkinabé adolescent girls predicts malaria risk in the following rainy season. Nutrients. 2020;12(5).
12. Thipubon P, Uthaipibull C, Kamchonwongpaisan S, Tipsuwan W, Srichairatanakool S. Inhibitory effect of novel iron chelator, 1-(N-acetyl-6-aminohexyl)-3-hydroxy-2-methylpyridin-4-one (CM1) and green tea extract on growth of *Plasmodium falciparum*. Malaria J. 2015;14(1):382.
13. Scholl PF, Tripathi AK, Sullivan DJ. Bioavailable iron and heme metabolism in *Plasmodium falciparum*. Curr Top Microbiol Immunol. 2005;295:293-324.
14. Brancucci NMB, Gerdt JP, Wang C, De Niz M, Philip N, Adapa SR, et al. Lysophosphatidylcholine regulates sexual stage differentiation in the human malaria parasite *Plasmodium falciparum*. Cell. 2017;171(7):1532-44.e15.
15. Chou ES, Abidi SZ, Teye M, Leliwa-Sytek A, Rask TS, Cobbold SA, et al. A high parasite density environment induces transcriptional changes and cell death in *Plasmodium falciparum* blood stages. FEBS J. 2018;285(5):848-70.
16. Mancio-Silva L, Slavic K, Grilo Ruivo MT, Grosso AR, Modrzynska KK, Vera IM, et al. Nutrient sensing modulates malaria parasite virulence. Nature. 2017;547(7662):213-6.
17. Sigala PA, Goldberg DE. The peculiarities and paradoxes of *Plasmodium* heme metabolism. Annu Rev Microbiol. 2014;68:259-78.
18. Mach J, Sutak R. Iron in parasitic protists – from uptake to storage and where we can interfere. Metallomics. 2020;12(9):1335-47.
19. Darbari D, Loyevsky M, Gordeuk V, Kark JA, Castro O, Rana S, et al. Fluorescence measurements of the labile iron pool of sickle erythrocytes. Blood. 2003;102(1):357-64.
20. Loyevsky M, John C, Dickens B, Hu V, Miller JH, Gordeuk VR. Chelation of iron within the erythrocytic *Plasmodium falciparum* parasite by iron chelators. Mol Biochem Parasitol. 1999;101(1-2):43-59.
21. Becker K, Tilley L, Vennerstrom JL, Roberts D, Rogerson S, Ginsburg H. Oxidative stress in malaria parasite-infected erythrocytes: host–parasite interactions. Int J Parasitol. 2004;34(2):163-89.
22. Wunderlich J, Rohrbach P, Dalton JP. The malaria digestive vacuole. Front Biosci (Schol Ed). 2012;4:1424-48.
23. Kloehn J, Harding CR, Soldati-Favre D. Supply and demand - heme synthesis, salvage and utilization by Apicomplexa. FEBS J. 2020;288(2):382-404.
24. Huang G, Ulrich PN, Storey M, Johnson D, Tischer J, Tovar JA, et al. Proteomic analysis of the acidocalcisome, an organelle conserved from bacteria to human cells. PLoS Pathog. 2014;10(12):e1004555.
25. Ruiz FA, Luo S, Moreno SN, Docampo R. Polyphosphate content and fine structure of acidocalcisomes of *Plasmodium falciparum*. Microsc Microanal. 2004;10(5):563-7.
26. Magowan C, Brown JT, Liang J, Heck J, Coppel RL, Mohandas N, et al. Intracellular structures of normal and aberrant *Plasmodium falciparum* malaria parasites imaged by soft x-ray microscopy. Proc Natl Acad Sci U S A. 1997;94(12):6222-7.
27. de Oliveira LS, Alborghetti MR, Carneiro RG, Bastos IMD, Amino R, Grellier P, et al. Calcium in the backstage of malaria parasite biology. Front Cell Infect Microbiol. 2021;11:708834.
28. Wunderlich J. Updated list of transport proteins in *Plasmodium falciparum*. Front Cell Infect Microbiol. 2022;12:926541.
29. Altschul SF, Madden TL, Schäffer AA, Zhang J, Zhang Z, Miller W, et al. Gapped BLAST and PSI-BLAST: a new generation of protein database search programs. Nucleic Acids Res. 1997;25(17):3389-402.
30. Slavic K, Krishna S, Lahree A, Bouyer G, Hanson KK, Vera I, et al. A vacuolar iron-transporter homologue acts as a detoxifier in *Plasmodium*. Nat Commun. 2016;7:10403.
31. Sharma P, Tóth V, Hyland EM, Law CJ. Characterization of the substrate binding site of an iron detoxifying membrane transporter from *Plasmodium falciparum*. Malar J. 2021;20(1):295.
32. Labarbuta P, Duckett K, Botting CH, Chahrour O, Malone J, Dalton JP, et al. Recombinant vacuolar iron transporter family homologue *Pf*VIT from human malaria-causing *Plasmodium falciparum* is a Fe^{2+}/H^{+}exchanger. Sci Rep. 2017;7:42850.

33. Waller KL, Muhle RA, Ursos LM, Horrocks P, Verdier-Pinard D, Sidhu AB, et al. Chloroquine resistance modulated *in vitro* by expression levels of the *Plasmodium falciparum* chloroquine resistance transporter. J Biol Chem. 2003;278(35):33593-601.
34. Wichers JS, Mesén-Ramírez P, Fuchs G, Yu-Strzelczyk J, Stäcker J, von Thien H, et al. PMRT1, a *Plasmodium*-specific parasite plasma membrane transporter, is essential for asexual and sexual blood stage development. mBio. 2022;13(2):e00623-22.
35. Bakouh N, Bellanca S, Nyboer B, Moliner Cubel S, Karim Z, Sanchez CP, et al. Iron is a substrate of the *Plasmodium falciparum* chloroquine resistance transporter *Pf*CRT in Xenopus oocytes. J Biol Chem. 2017;292(39):16109-21.
36. Martin RE, Henry RI, Abbey JL, Clements JD, Kirk K. The 'permeome' of the malaria parasite: an overview of the membrane transport proteins of *Plasmodium falciparum*. Genome Biol. 2005;6(3):R26.
37. Brazzolotto X, Pierrel F, Pelosi L. Three conserved histidine residues contribute to mitochondrial iron transport through mitoferrins. Biochem J. 2014;460(1):79-89.
38. Mühlenhoff U, Stadler JA, Richhardt N, Seubert A, Eickhorst T, Schweyen RJ, et al. A specific role of the yeast mitochondrial carriers Mrs3/4p in mitochondrial iron acquisition under iron-limiting conditions. J Biol Chem. 2003;278(42):40612-20.
39. Froschauer EM, Schweyen RJ, Wiesenberger G. The yeast mitochondrial carrier proteins Mrs3p/Mrs4p mediate iron transport across the inner mitochondrial membrane. Biochim Biophys Acta. 2009;1788(5):1044-50.
40. Mather MW, Henry KW, Vaidya AB. Mitochondrial drug targets in apicomplexan parasites. Curr Drug Targets. 2007;8(1):49-60.
41. Aschemeyer S, Qiao B, Stefanova D, Valore EV, Sek AC, Ruwe TA, et al. Structure-function analysis of ferroportin defines the binding site and an alternative mechanism of action of hepcidin. Blood. 2018;131(8):899-910.
42. Billesbølle CB, Azumaya CM, Kretsch RC, Powers AS, Gonen S, Schneider S, et al. Structure of hepcidin-bound ferroportin reveals iron homeostatic mechanisms. Nature. 2020.
43. Knovich MA, Storey JA, Coffman LG, Torti SV, Torti FM. Ferritin for the clinician. Blood Rev. 2009;23(3):95-104.
44. Nemeth E, Tuttle MS, Powelson J, Vaughn MB, Donovan A, Ward DM, et al. Hepcidin regulates cellular iron efflux by binding to ferroportin and inducing its internalization. Science. 2004;306(5704):2090-3.
45. Petrat F, Rauen U, de Groot H. Determination of the chelatable iron pool of isolated rat hepatocytes by digital fluorescence microscopy using the fluorescent probe, phen green SK. Hepatology. 1999;29(4):1171-9.
46. Lemieux JE, Gomez-Escobar N, Feller A, Carret C, Amambua-Ngwa A, Pinches R, et al. Statistical estimation of cell-cycle progression and lineage commitment in *Plasmodium falciparum* reveals a homogeneous pattern of transcription in *ex vivo* culture. Proc Natl Acad Sci U S A. 2009;106(18):7559-64.
47. Broadbent KM, Broadbent JC, Ribacke U, Wirth D, Rinn JL, Sabeti PC. Strand-specific RNA sequencing in *Plasmodium falciparum* malaria identifies developmentally regulated long non-coding RNA and circular RNA. BMC Genomics. 2015;16(1):454.
48. Wichers JS, Scholz JAM, Strauss J, Witt S, Lill A, Ehnold LI, et al. Dissecting the gene expression, localization, membrane topology, and function of the *Plasmodium falciparum* STEVOR protein family. mBio. 2019;10(4).
49. Stewart LB, Diaz-Ingelmo O, Claessens A, Abugri J, Pearson RD, Goncalves S, et al. Intrinsic multiplication rate variation and plasticity of human blood stage malaria parasites. Commun Biol. 2020;3(1):624.
50. Benjamini Y, Hochberg Y. Controlling the false discovery rate: a practical and powerful approach to multiple Testing. J Royal Stat Soc Ser B. 1995;57(1):289-300.
51. Abrahamian M, Ah-Fong AM, Davis C, Andreeva K, Judelson HS. Gene expression and silencing studies in *Phytophthora infestans* reveal infection-specific nutrient transporters and a role for the nitrate reductase pathway in plant pathogenesis. PLoS Pathog. 2016;12(12):e1006097.
52. Küpper H, Kochian LV. Transcriptional regulation of metal transport genes and mineral nutrition during acclimatization to cadmium and zinc in the Cd/Zn hyperaccumulator, *Thlaspi caerulescens* (Ganges population). New Phytol. 2010;185(1):114-29.
53. Sarkans U, Gostev M, Athar A, Behrangi E, Melnichuk O, Ali A, et al. The BioStudies database - one stop shop for all data supporting a life sciences study. Nucleic Acids Res. 2018;46(D1):D1266-D70.

54. Bozdech Z, Llinás M, Pulliam BL, Wong ED, Zhu J, DeRisi JL. The transcriptome of the intraerythrocytic developmental cycle of *Plasmodium falciparum*. PLoS Biol. 2003;1(1):E5.
55. Kidgell C, Volkman SK, Daily J, Borevitz JO, Plouffe D, Zhou Y, et al. A systematic map of genetic variation in *Plasmodium falciparum*. PLoS Pathog. 2006;2(6):e57.
56. Raudvere U, Kolberg L, Kuzmin I, Arak T, Adler P, Peterson H, et al. g:Profiler: a web server for functional enrichment analysis and conversions of gene lists (2019 update). Nucleic Acids Res. 2019;47(W1):W191-W8.
57. Sloan MA, Aghabi D, Harding CR. Orchestrating a heist: uptake and storage of metals by apicomplexan parasites. Microbiology (Reading). 2021;167(12).
58. Loyevsky M, LaVaute T, Allerson CR, Stearman R, Kassim OO, Cooperman S, et al. An IRP-like protein from *Plasmodium falciparum* binds to a mammalian iron-responsive element. Blood. 2001;98(8):2555-62.
59. Hodges M, Yikilmaz E, Patterson G, Kasvosve I, Rouault TA, Gordeuk VR, et al. An iron regulatory-like protein expressed in *Plasmodium falciparum* displays aconitase activity. Mol Biochem Parasitol. 2005;143(1):29-38.
60. Kuhn Y, Sanchez CP, Ayoub D, Saridaki T, Van Dorsselaer A, Lanzer M. Trafficking of the phosphoprotein PfCRT to the digestive vacuolar membrane in *Plasmodium falciparum*. Traffic. 2010;11(2):236-49.
61. Edayé S, Georges E. Characterization of native PfABCG protein in *Plasmodium falciparum*. Biochem Pharmacol. 2015;97(2):137-46.
62. Lerch A, Koepfli C, Hofmann NE, Messerli C, Wilcox S, Kattenberg JH, et al. Development of amplicon deep sequencing markers and data analysis pipeline for genotyping multi-clonal malaria infections. BMC Genomics. 2017;18(1):864.
63. Spork S, Hiss JA, Mandel K, Sommer M, Kooij TW, Chu T, et al. An unusual ERAD-like complex is targeted to the apicoplast of *Plasmodium falciparum*. Eukaryot Cell. 2009;8(8):1134-45.
64. Zhang M, Wang C, Otto TD, Oberstaller J, Liao X, Adapa SR, et al. Uncovering the essential genes of the human malaria parasite *Plasmodium falciparum* by saturation mutagenesis. Science. 2018;360(6388):eaap7847.
65. Prommana P, Uthaipibull C, Wongsombat C, Kamchonwongpaisan S, Yuthavong Y, Knuepfer E, et al. Inducible knockdown of *Plasmodium* gene expression using the *glmS* ribozyme. PLoS One. 2013;8(8):e73783.
66. Jumper J, Evans R, Pritzel A, Green T, Figurnov M, Ronneberger O, et al. Highly accurate protein structure prediction with AlphaFold. Nature. 2021;596(7873):583-9.
67. Varadi M, Anyango S, Deshpande M, Nair S, Natassia C, Yordanova G, et al. AlphaFold Protein Structure Database: massively expanding the structural coverage of protein-sequence space with high-accuracy models. Nucleic Acids Res. 2022;50(D1):D439-D44.
68. Evans R, O'Neill M, Pritzel A, Antropova N, Senior A, Green T, et al. Protein complex prediction with AlphaFold-Multimer. bioRxiv. 2022.
69. Kato T, Kumazaki K, Wada M, Taniguchi R, Nakane T, Yamashita K, et al. Crystal structure of plant vacuolar iron transporter VIT1. Nat Plants. 2019;5(3):308-15.
70. Saier MH, Jr., Reddy VS, Tsu BV, Ahmed MS, Li C, Moreno-Hagelsieb G. The Transporter Classification Database (TCDB): recent advances. Nucleic Acids Res. 2016;44(D1):D372-D9.
71. Pang C, Chai J, Zhu P, Shanklin J, Liu Q. Structural mechanism of intracellular autoregulation of zinc uptake in ZIP transporters. Nat Commun. 2023;14(1):3404.
72. Kim J, Tan YZ, Wicht KJ, Erramilli SK, Dhingra SK, Okombo J, et al. Structure and drug resistance of the *Plasmodium falciparum* transporter PfCRT. Nature. 2019.
73. Ehrnstorfer IA, Geertsma ER, Pardon E, Steyaert J, Dutzler R. Crystal structure of a SLC11 (NRAMP) transporter reveals the basis for transition-metal ion transport. Nat Struct Mol Biol. 2014;21(11):990-6.
74. Meerstein-Kessel L, Venhuizen J, Garza D, Proellochs NI, Vos EJ, Obiero JM, et al. Novel insights from the *Plasmodium falciparum* sporozoite-specific proteome by probabilistic integration of 26 studies. PLoS Comput Biol. 2021;17(4):e1008067.
75. Gligorijević V, Renfrew PD, Kosciolek T, Leman JK, Berenberg D, Vatanen T, et al. Structure-based protein function prediction using graph convolutional networks. Nat Commun. 2021;12(1):3168.
76. Goheen MM, Bah A, Wegmüller R, Verhoef H, Darboe B, Danso E, et al. Host iron status and erythropoietic response to iron supplementation determines susceptibility to the RBC stage of falciparum malaria during pregnancy. Sci Rep. 2017;7(1):17674.
77. Muriuki JM, Mentzer AJ, Mitchell R, Webb EL, Etyang AO, Kyobutungi C, et al. Malaria is a cause of iron deficiency in African children. Nat Med. 2021;27(4):653-8.

78. Kim CH, Kim HK, Bae SJ, Park JY, Lee KU. Association of elevated serum ferritin concentration with insulin resistance and impaired glucose metabolism in Korean men and women. Metabolism. 2011;60(3):414-20.
79. Newhouse IJ, Clement DB, Lai C. Effects of iron supplementation and discontinuation on serum copper, zinc, calcium, and magnesium levels in women. Med Sci Sports Exerc. 1993;25(5):562-71.
80. Milner DA, Jr., Pochet N, Krupka M, Williams C, Seydel K, Taylor TE, et al. Transcriptional profiling of *Plasmodium falciparum* parasites from patients with severe malaria identifies distinct low vs. high parasitemic clusters. PLoS One. 2012;7(7):e40739.
81. Thomson-Luque R, Votborg-Novél L, Ndovie W, Andrade CM, Niangaly M, Attipa C, et al. *Plasmodium falciparum* transcription in different clinical presentations of malaria associates with circulation time of infected erythrocytes. Nat Commun. 2021;12(1):4711.
82. Lee HJ, Georgiadou A, Walther M, Nwakanma D, Stewart LB, Levin M, et al. Integrated pathogen load and dual transcriptome analysis of systemic host-pathogen interactions in severe malaria. Sci Transl Med. 2018;10(447).
83. Muckenthaler MU, Rivella S, Hentze MW, Galy B. A red carpet for iron metabolism. Cell. 2017;168(3):344-61.
84. Cercamondi CI, Egli IM, Ahouandjinou E, Dossa R, Zeder C, Salami L, et al. Afebrile *Plasmodium falciparum* parasitemia decreases absorption of fortification iron but does not affect systemic iron utilization: a double stable-isotope study in young Beninese women. Am J Clin Nutr. 2010;92(6):1385-92.
85. Duraisingh MT, Skillman KM. Epigenetic variation and regulation in malaria parasites. Annu Rev Microbiol. 2018;72:355-75.
86. Ramos-Alonso L, Romero AM, Martínez-Pastor MT, Puig S. Iron regulatory mechanisms in *Saccharomyces cerevisiae*. Front Microbiol. 2020;11:582830.
87. Gilabert Carbajo C, Cornell LJ, Madbouly Y, Lai Z, Yates PA, Tinti M, et al. Novel aspects of iron homeostasis in pathogenic bloodstream form *Trypanosoma brucei*. PLOS Pathogens. 2021;17(6):e1009696.
88. Wang J, Pantopoulos K. Regulation of cellular iron metabolism. Biochem J. 2011;434(3):365-81.
89. Bushell E, Gomes AR, Sanderson T, Anar B, Girling G, Herd C, et al. Functional profiling of a *Plasmodium* genome reveals an abundance of essential genes. Cell. 2017;170(2):260-72.e8.
90. Aghabi D, Sloan M, Gill G, Hartmann E, Antipova O, Dou Z, et al. The vacuolar iron transporter mediates iron detoxification in *Toxoplasma gondii*. Nat Commun. 2023;14(1):3659.
91. Li L, Murdock G, Bagley D, Jia X, Ward DM, Kaplan J. Genetic Dissection of a Mitochondria-Vacuole Signaling Pathway in Yeast Reveals a Link between Chronic Oxidative Stress and Vacuolar Iron Transport. J Biol Chem. 2010;285(14):10232-42.
92. Schnell U, Dijk F, Sjollema KA, Giepmans BN. Immunolabeling artifacts and the need for live-cell imaging. Nat Methods. 2012;9(2):152-8.
93. Mathew R, Wunderlich J, Thivierge K, Cwiklinski K, Dumont C, Tilley L, et al. Biochemical and cellular characterisation of the *Plasmodium falciparum* M1 alanyl aminopeptidase (*Pf*M1AAP) and M17 leucyl aminopeptidase (*Pf*M17LAP). Sci Rep. 2021;11(1):2854.
94. Schembri L, Dalibart R, Tomasello F, Legembre P, Ichas F, De Giorgi F. The HA tag is cleaved and loses immunoreactivity during apoptosis. Nat Methods. 2007;4(2):107-8.
95. Sahu T, Boisson B, Lacroix C, Bischoff E, Richier Q, Formaglio P, et al. ZIPCO, a putative metal ion transporter, is crucial for *Plasmodium* liver□stage development. EMBO Mol Med. 2014;6(11):1387-97.
96. Sidik SM, Huet D, Ganesan SM, Huynh MH, Wang T, Nasamu AS, et al. A genome-wide CRISPR screen in *Toxoplasma* identifies essential apicomplexan genes. Cell. 2016;166(6):1423-35.e12.
97. Shrivastava D, Jha A, Kabrambam R, Vishwakarma J, Mitra K, Ramachandran R, et al. *Plasmodium falciparum* ZIP1 is a zinc-selective transporter with stage-dependent targeting to the apicoplast and plasma membrane in erythrocytic parasites. ACS Infect Dis. 2024;10(1):155-69.
98. Rohrbach P, Friedrich O, Hentschel J, Plattner H, Fink RH, Lanzer M. Quantitative calcium measurements in subcellular compartments of *Plasmodium falciparum*-infected erythrocytes. J Biol Chem. 2005;280(30):27960-9.
99. Bozzi AT, Bane LB, Weihofen WA, Singharoy A, Guillen ER, Ploegh HL, et al. Crystal structure and conformational change mechanism of a bacterial Nramp-family divalent metal transporter. Structure. 2016;24(12):2102-14.

100. Bozzi AT, Bane LB, Zimanyi CM, Gaudet R. Unique structural features in an Nramp metal transporter impart substrate-specific proton cotransport and a kinetic bias to favor import. J Gen Physiol. 2019;151(12):1413-29.
101. Smith EC, Limbach KJ, Rangel N, Oda K, Bolton JS, Du M, et al. Novel malaria antigen *Plasmodium yoelii* E140 induces antibody-mediated sterile protection in mice against malaria challenge. PLoS One. 2020;15(5):e0232234.
102. Trager W, Jensen JB. Human malaria parasites in continuous culture. Science. 1976;193(4254):673-5.
103. Malleret B, Claser C, Ong AS, Suwanarusk R, Sriprawat K, Howland SW, et al. A rapid and robust tri-color flow cytometry assay for monitoring malaria parasite development. Sci Rep. 2011;1:118.
104. Rivadeneira EM, Wasserman M, Espinal CT. Separation and concentration of schizonts of *Plasmodium falciparum* by Percoll gradients. J Protozool. 1983;30(2):367-70.
105. Lambros C, Vanderberg JP. Synchronization of *Plasmodium falciparum* erythrocytic stages in culture. J Parasitol. 1979;65(3):418-20.
106. Birnbaum J, Flemming S, Reichard N, Soares AB, Mesén-Ramírez P, Jonscher E, et al. A genetic system to study *Plasmodium falciparum* protein function. Nat Methods. 2017;14(4):450-6.
107. Burda PC, Crosskey T, Lauk K, Zurborg A, Söhnchen C, Liffner B, et al. Structure-based identification and functional characterization of a lipocalin in the malaria parasite *Plasmodium falciparum*. Cell Rep. 2020;31(12):107817.
108. Moon RW, Hall J, Rangkuti F, Ho YS, Almond N, Mitchell GH, et al. Adaptation of the genetically tractable malaria pathogen *Plasmodium knowlesi* to continuous culture in human erythrocytes. Proc Natl Acad Sci U S A. 2013;110(2):531-6.
109. Schindelin J, Arganda-Carreras I, Frise E, Kaynig V, Longair M, Pietzsch T, et al. Fiji: an open-source platform for biological-image analysis. Nat Methods. 2012;9(7):676-82.
110. Andrews S. FastQC: a quality control tool for high throughput sequence data. Babraham Bioinformatics, Babraham Institute, Cambridge, UK; 2010.
111. Martin M. Cutadapt removes adapter sequences from high-throughput sequencing reads. EMBnet J. 2011;17(1):10-2.
112. Aurrecoechea C, Brestelli J, Brunk BP, Dommer J, Fischer S, Gajria B, et al. PlasmoDB: a functional genomic database for malaria parasites. Nucleic Acids Res. 2009;37(Database issue):D539-D43.
113. Dobin A, Davis CA, Schlesinger F, Drenkow J, Zaleski C, Jha S, et al. STAR: ultrafast universal RNA-seq aligner. Bioinformatics. 2013;29(1):15-21.
114. Ewels P, Magnusson M, Lundin S, Käller M. MultiQC: summarize analysis results for multiple tools and samples in a single report. Bioinformatics. 2016;32(19):3047-8.
115. Liao Y, Smyth GK, Shi W. featureCounts: an efficient general purpose program for assigning sequence reads to genomic features. Bioinformatics. 2014;30(7):923-30.
116. Liao Y, Smyth GK, Shi W. The Subread aligner: fast, accurate and scalable read mapping by seed-and-vote. Nucleic Acids Res. 2013;41(10):e108.
117. Li H, Handsaker B, Wysoker A, Fennell T, Ruan J, Homer N, et al. The Sequence Alignment/Map format and SAMtools. Bioinformatics. 2009;25(16):2078-9.
118. Robinson MD, McCarthy DJ, Smyth GK. edgeR: a Bioconductor package for differential expression analysis of digital gene expression data. Bioinformatics. 2010;26(1):139-40.
119. Sanderson T, Rayner JC. PhenoPlasm: a database of disruption phenotypes for malaria parasite genes. Wellcome Open Res. 2017;2:45.
120. Blighe K, Rana S, Lewis M. EnhancedVolcano: Publication-ready volcano plots with enhanced colouring and labeling. R package version. 2022;1.15.
121. Supek F, Bošnjak M, Škunca N, Šmuc T. REVIGO summarizes and visualizes long lists of gene ontology terms. PLoS One. 2011;6(7):e21800.
122. Crameri F, Shephard GE, Heron PJ. The misuse of colour in science communication. Nat Commun. 2020;11(1):5444.
123. Goddard TD, Huang CC, Meng EC, Pettersen EF, Couch GS, Morris JH, et al. UCSF ChimeraX: Meeting modern challenges in visualization and analysis. Protein Sci. 2018;27(1):14-25.
124. Meng EC, Pettersen EF, Couch GS, Huang CC, Ferrin TE. Tools for integrated sequence-structure analysis with UCSF Chimera. BMC Bioinformatics. 2006;7:339.
125. Birnbaum J, Scharf S, Schmidt S, Jonscher E, Hoeijmakers WAM, Flemming S, et al. A Kelch13-defined endocytosis pathway mediates artemisinin resistance in malaria parasites. Science. 2020;367(6473):51-9.

126. Ward DM, Kaplan J. Ferroportin-mediated iron transport: Expression and regulation. Biochimica et Biophysica Acta (BBA) - Molecular Cell Research. 2012;1823(9):1426-33.
127. Mesén-Ramírez P, Bergmann B, Elhabiri M, Zhu L, von Thien H, Castro-Peña C, et al. The parasitophorous vacuole nutrient channel is critical for drug access in malaria parasites and modulates the artemisinin resistance fitness cost. Cell Host Microbe. 2021.
128. Sassmannshausen J, Pradel G, Bennink S. Perforin-like proteins of apicomplexan parasites. Front Cell Infect Microbiol. 2020;10:578883.
129. Jonker JW, Buitelaar M, Wagenaar E, Van Der Valk MA, Scheffer GL, Scheper RJ, et al. The breast cancer resistance protein protects against a major chlorophyll-derived dietary phototoxin and protoporphyria. Proc Natl Acad Sci U S A. 2002;99(24):15649-54.
130. Ahiya AI, Bhatnagar S, Morrisey JM, Beck JR, Vaidya AB. Dramatic consequences of reducing erythrocyte membrane cholesterol on *Plasmodium falciparum*. Microbiol Spectr. 2022;10(1):e0015822.
131. Schmidt O, Pfanner N, Meisinger C. Mitochondrial protein import: from proteomics to functional mechanisms. Nat Rev Mol Cell Biol. 2010;11(9):655-67.
132. Sheiner L, Soldati-Favre D. Protein trafficking inside *Toxoplasma gondii*. Traffic. 2008;9(5):636-46.
133. Moonah S, Sanders NG, Persichetti JK, Sullivan DJ, Jr. Erythrocyte lysis and *Xenopus laevis* oocyte rupture by recombinant *Plasmodium falciparum* hemolysin III. Eukaryot Cell. 2014;13(10):1337-45.
134. Lim L, Linka M, Mullin KA, Weber AP, McFadden GI. The carbon and energy sources of the non-photosynthetic plastid in the malaria parasite. FEBS Lett. 2010;584(3):549-54.
135. Hayashi M, Yamada H, Mitamura T, Horii T, Yamamoto A, Moriyama Y. Vacuolar H^+-ATPase localized in plasma membranes of malaria parasite cells, *Plasmodium falciparum*, is involved in regional acidification of parasitized erythrocytes. J Biol Chem. 2000;275(44):34353-8.
136. Friedrich O, Reiling SJ, Wunderlich J, Rohrbach P. Assessment of *Plasmodium falciparum* PfMDR1 transport rates using Fluo-4. J Cell Mol Med. 2014;18(9):1851-62.
137. Marapana DS, Dagley LF, Sandow JJ, Nebl T, Triglia T, Pasternak M, et al. Plasmepsin V cleaves malaria effector proteins in a distinct endoplasmic reticulum translocation interactome for export to the erythrocyte. Nat Microbiol. 2018;3(9):1010-22.
138. Blume M, Hliscs M, Rodriguez-Contreras D, Sanchez M, Landfear S, Lucius R, et al. A constitutive pan-hexose permease for the *Plasmodium* life cycle and transgenic models for screening of antimalarial sugar analogs. Faseb j. 2011;25(4):1218-29.
139. Spillman Natalie J, Allen Richard JW, McNamara Case W, Yeung Bryan KS, Winzeler Elizabeth A, Diagana Thierry T, et al. Na^+ regulation in the malaria parasite *Plasmodium falciparum* involves the cation ATPase *Pf*ATP4 and is a target of the spiroindolone antimalarials. Cell Host Microbe. 2013;13(2):227-37.
140. Boucher MJ, Ghosh S, Zhang L, Lal A, Jang SW, Ju A, et al. Integrative proteomics and bioinformatic prediction enable a high-confidence apicoplast proteome in malaria parasites. PLoS Biol. 2018;16(9):e2005895.
141. van Esveld SL, Meerstein-Kessel L, Boshoven C, Baaij JF, Barylyuk K, Coolen JPM, et al. A prioritized and validated resource of mitochondrial proteins in *Plasmodium* identifies unique biology. mSphere. 2021;6(5):e0061421.
142. Wichers JS, van Gelder C, Fuchs G, Ruge JM, Pietsch E, Ferreira JL, et al. Characterization of Apicomplexan Amino Acid Transporters (ApiATs) in the malaria parasite *Plasmodium falciparum*. mSphere. 2021;6(6):e00743-21.
143. Gardner MJ, Hall N, Fung E, White O, Berriman M, Hyman RW, et al. Genome sequence of the human malaria parasite *Plasmodium falciparum*. Nature. 2002;419(6906):498-511.
144. Martin RE. The transportome of the malaria parasite. Biol Rev Camb Philos Soc. 2020;95(2):305-32.
145. Carter NS, Ben Mamoun C, Liu W, Silva EO, Landfear SM, Goldberg DE, et al. Isolation and functional characterization of the *Pf*NT1 nucleoside transporter gene from *Plasmodium falciparum*. J Biol Chem. 2000;275(14):10683-91.
146. Kenthirapalan S, Waters AP, Matuschewski K, Kooij TW. Copper-transporting ATPase is important for malaria parasite fertility. Mol Microbiol. 2014;91(2):315-25.
147. Park DJ, Lukens AK, Neafsey DE, Schaffner SF, Chang HH, Valim C, et al. Sequence-based association and selection scans identify drug resistance loci in the *Plasmodium falciparum* malaria parasite. Proc Natl Acad Sci U S A. 2012;109(32):13052-67.

148. Sayers CP, Mollard V, Buchanan HD, McFadden GI, Goodman CD. A genetic screen in rodent malaria parasites identifies five new apicoplast putative membrane transporters, one of which is essential in human malaria parasites. Cell Microbiol. 2018;20(1):e12789.
149. Cowell AN, Istvan ES, Lukens AK, Gomez-Lorenzo MG, Vanaerschot M, Sakata-Kato T, et al. Mapping the malaria parasite druggable genome by using *in vitro* evolution and chemogenomics. Science. 2018;359(6372):191-9.
150. Gupta Y, Sharma N, Singh S, Romero JG, Rajendran V, Mogire RM, et al. The multistage antimalarial compound calxinin perturbates *P. falciparum* Ca^{2+} homeostasis by targeting a unique ion channel. Pharmaceutics. 2022;14(7):1371.
151. Nozawa A, Ito D, Ibrahim M, Santos HJ, Tsuboi T, Tozawa Y. Characterization of mitochondrial carrier proteins of malaria parasite *Plasmodium falciparum* based on *in vitro* translation and reconstitution. Parasitol Int. 2020;79:102160.
152. Agrawal S, Striepen B. More membranes, more proteins: complex protein import mechanisms into secondary plastids. Protist. 2010;161(5):672-87.
153. Schureck MA, Darling JE, Merk A, Shao J, Daggupati G, Srinivasan P, et al. Malaria parasites use a soluble RhopH complex for erythrocyte invasion and an integral form for nutrient uptake. eLife. 2021;10:e65282.
154. Chitale M, Hawkins T, Park C, Kihara D. ESG: extended similarity group method for automated protein function prediction. Bioinformatics. 2009;25(14):1739-45.
155. Stanway RR, Bushell E, Chiappino-Pepe A, Roques M, Sanderson T, Franke-Fayard B, et al. Genome-scale identification of essential metabolic processes for targeting the *Plasmodium* liver stage. Cell. 2019;179(5):1112-28.e26.
156. Ecker A, Lakshmanan V, Sinnis P, Coppens I, Fidock DA. Evidence that mutant *Pf*CRT facilitates the transmission to mosquitoes of chloroquine-treated *Plasmodium* gametocytes. J Infect Dis. 2011;203(2):228-36.

Figures:

Figure 1: Effects of the iron status of the blood donor and of hepcidin on (A) erythrocyte free iron levels, (B) *P. falciparum* 3D7 growth rates, (C) DNA content per mature schizont, and (D) the number of merozoites per mature schizont.

The relative free iron level and DNA content per cell were assessed by measuring the mean fluorescence intensity (MFI) of Phen Green SK or SYBR Green I compared to control (Ctrl, untreated, normal hemoglobin level) using flow cytometry. 0.7 µM hepcidin (Hep) was chosen as a concentration reported to reduce binding of ferrous iron to the erythrocyte iron exporter ferroportin by 50% in vitro (44). Parasite growth rates refer to the fold change in parasitemia after one intraerythrocytic developmental cycle in vitro relative to control as determined by flow cytometry with SYBR Green I (103). Mature schizonts were obtained by treating schizonts at 40 hpi with 1 mM compound 2 (4-[7-[(dimethylamino)methyl]-2-(4-fluorphenyl)imidazo[1,2-α]pyridine-3-yl]pyrimidin-2-amine) for 8 h. To count the number of merozoites, Giemsa-stained blood smears were analyzed microscopically and only single-infected cells with one digestive vacuole were considered. Means and 95% confidence intervals (indicated by error bars) are shown. Statistical significance was calculated with two-tailed unpaired *t* tests with Welch's correction for unequal variances and adjusted with the Holm-Šídák method for multiple comparisons except for merozoite numbers, which were compared using Mann-Whitney test. N represents the number of parasites and n the number of independent experiments.

Figure 2: Differential expression of *P. falciparum* 3D7 genes under various iron conditions.

Parasites were cultured with erythrocytes from an individual with high, medium (healthy) or low iron status (experiment 1) or with red blood cells from another healthy donor in the presence or absence of 0.7 µM hepcidin (experiment 2). Samples were harvested at the ring and trophozoite stage (6 – 9 and 26 – 29 hours post invasion, hpi) with three biological replicates per time point and condition. The maximum likelihood estimation (MLE) of the average developmental age of the parasites for each condition and time point (**A**) was calculated using an algorithm developed by Avi Feller and Jacob Lemieux (46). CI, confidence interval. The volcano plots (**B** and **D**) show transcriptional changes of all parasite genes. Red dots indicate significantly ($P < 0.05$, exact test for negative binomial distribution) upregulated genes ($\log_2$ (fold change) ≥ 0.2), blue dots stand for significantly downregulated genes ($\log_2$ (fold change) ≤ -0.2), while grey dots represent genes that did not significantly differ in transcription under the conditions described ($P \geq 0.05$ and / or $-0.2 < \log_2$ (fold change) < 0.2). Differentially expressed genes encoding putative iron transporters (see Table 1) are labeled. Panels **C** and **E** show the enrichment of Gene Ontology (GO), Kyoto Encyclopedia of Genes and Genomes (KEGG) and Reactome (REAC) terms among significantly regulated genes excluding *var, stevor* and *rifin* gene families at the two time points. The functional terms were summarized using REVIGO (121) to remove redundancies, represented by circles and plotted according to the significance of their enrichment ($-\log_{10}$ (adjusted P), hypergeometric test). The size of the circle is proportional to the number of differentially regulated genes in the dataset that are associated with the respective term, while the color stands for the fold enrichment. The gray dashed line indicates the threshold of the adjusted P value ($-\log_{10} 0.05 = 1.3$).

Figure 3: Subcellular localization of four putative iron transport proteins.

Representative erythrocytes infected with *P. falciparum* 3D7 parasites endogenously expressing GFP-tagged *Pf*MRS3 (**A**), *Pf*VIT (**B**), *Pf*ZIPCO (**C**) or *Pf*E140 (**D**) were additionally stained with the fluorescent dyes Hoechst-33342, MitoTracker Red, ER Tracker Red and/or LysoTracker Deep Red. Co-transfection with a construct that encodes the 60 N-terminal amino acids of acyl carrier protein (*Pf*ACP) tagged with mCherry (125) resulted in red fluorescence of the apicoplast. Live-cell images were taken under physiological conditions at 37°C using an SP8 confocal laser-scanning microscope (Leica). DIC, differential interference contrast. Scale bar, 2 µm.

Figure 4: *Pf*VIT and *Pf*E140 are important for *P. falciparum* growth and may be involved in intracellular iron homeostasis.

A Representative erythrocytes infected with *P. falciparum* 3D7 parasites that endogenously express a truncated version of *Pf*VIT or *Pf*ZIPCO tagged with GFP (green). **B** Growth rates of knockout parasite lines generated. **C** Reduction of *Pf*E140-GFP fluorescence (green) in live 3D7 parasites caused by *glmS*-mediated knockdown that was induced by treatment with 2.5 mM glucosamine (GlcN) for 36 h compared to untreated control (Ctrl). **D** Total parasite fluorescence intensities were quantified as background-corrected integrated densities using ImageJ version 2.9.0/1.53t (109) and compared using Mann-Whitney test. **E** The size of the parasites was measured as the area of the region of interest and compared using equal variance unpaired *t* test. **F** Conditional knockdown of *Pf*E140 induced by treatment with 2.5 mM GlcN results in a growth defect during asexual blood stage development. Live parasites were stained with Hoechst-33342 (blue) and imaged under physiological conditions at 37°C using an SP8 confocal laser-scanning microscope (Leica). DIC, differential interference contrast. Scale bar, 2 µm. Error bars represent 95% confidence intervals of the mean, N the number of parasites analyzed, n the number of independent experiments and Hep treatment with 0.7 µM hepcidin. Growth rates refer to the fold change in parasitemia after two intraerythrocytic developmental cycles in vitro relative to untreated wild-type 3D7 parasites (WT) as determined by flow cytometry with SYBR Green I (103). Statistical significance of growth differences was calculated with two-tailed unpaired *t* tests with Welch's correction for unequal variances and adjusted with the Holm-Šídák method for multiple comparisons.

Figure 5: Predicted structures of putative iron transporters identified in *P. falciparum* as viewed from the membrane plane.

A Predicted protein structures with per-residue pLDDT (predicted local distance difference test) confidence scores on a scale from 0 to 100, where blue represents high and red low confidence, respectively. The experimentally determined structure of *Pf*CRT is shown in gray. **B** Molecular lipophilicity potential of the protein surfaces as implemented in UCSF ChimeraX; tan is hydrophobic and cyan hydrophilic. Dashed lines above and below the tan regions of all proteins indicate the respective membrane and disordered loops were removed for clarity. **C** Surface charge of the proteins with positively charged areas colored blue and negatively charged ones red. Putative cation-binding site are indicated with an asterisk and transport directions by arrows. *Pf*E140 likely forms a dimer but is shown as a monomer, as no predicted dimer structure could be obtained using AlphaFold2-multimer. The putative cation-binding sites for this protein are based on DeepFRI gradCAM scores for the functional term GO:0015075 "monoatomic ion transmembrane transporter activity" (Supplementary Fig. S5).

Figure 6: Iron homeostasis in a *P. falciparum*-infected erythrocyte.

The human blood plasma contains between 10 and 30 µM total Fe and the erythrocyte cytosol approximately 20 mM (19). However, only 2.5 – 4.7 µM of Fe^{2+} is bioavailable in an uninfected erythrocyte, and 1.5 – 1.8 µM in a *P. falciparum*-infected one (20). Human ferroportin (FPN) at the host cell surface (erythrocyte plasma membrane, EPM) exports free iron from the erythrocyte (126), the nutrient pore formed by *Pf*EXP1 and *Pf*EXP2 allows the passage of the ions through the parasitophorous vacuole membrane (PVM) (127). *Pf*E140 at the parasite plasma membrane (PPM) may mediate iron uptake iron into the parasite cytosol and the mitochondrial carrier protein *Pf*MRS3 likely translocates Fe^{2+} into the mitochondrion, a site of *de novo* heme biosynthesis. The digestive vacuole (DV) contains a high amount of total Fe as it is the site of hemoglobin degradation. The chloroquine resistance transporter (*Pf*CRT) and the natural resistance-associated macrophage protein (*Pf*NRAMP) were suggested to mediate proton-coupled export of Fe^{2+} from the DV into the parasite cytosol (35, 36). The vacuolar iron transporter (*Pf*VIT) may be involved in iron detoxification by transporting excess iron from the cytosol into cytoplasmic vesicles that may be acidocalcisomes, whereas *Pf*ZIPCO may release zinc and ferrous iron from these organelles under low-iron conditions (this study). Both acidocalcisomes and the DV are likely acidified by the plant-like H^+-pump V-ATPase, which can fuel secondary active transport processes (22, 27). Parasite-encoded proteins are shown in orange and human-encoded transporters in blue.

Table 1: *P. falciparum* transport proteins with differential gene expression under various iron conditions.

Putative and known transporter genes were filtered from differentially expressed genes in the described RNA-seq experiments using an updated list of *P. falciparum* transport proteins (28). The $\log_2$ (fold change) of gene expression at the ring stage (6 – 9 hours post invasion) and known or proposed functions are indicated for significantly regulated genes (exact $P < 0.05$) and putative iron transport proteins are highlighted in red. DV: digestive vacuole, EPM: erythrocyte plasma membrane, PPM: parasite plasma membrane.

Gene product and ID	$\log_2$ (fold change) high vs. low Fe	$\log_2$ (fold change) low Fe vs. control	$\log_2$(fold change) hepcidin vs. control	Known or putative function
PLP5 (PF3D7_0819200)	+ 0.49 (P = 0.0002)	n.s.	- 0.29 (P = 0.003)	Host cell permeabilization and rupture (128)
ABCG (PF3D7_1426500)	+ 0.45 (P = 0.02)	- 0.57 (P = 0.006)	n.s.	Putative metabolite exporter at PPM (61), human ortholog ABCG2 exports heme (129)
VP1 (PF3D7_1456800)	+ 0.39 (P = 0.0006)	- 0.34 (P = 0.004)	n.s.	Active H^+ export across PPM (130)
TOM7 (PF3D7_0823700)	+ 0.38 (P = 0.02)	n.s.	n.s.	Protein import across outer mitochondrial membrane (131, 132)
HlyIII (PF3D7_1455400)	+ 0.38 (P = 0.0009)	n.s.	n.s.	Forms pore (~3.2 nm) for solutes and ions in EPM (133)
TPT (PF3D7_0508300)	+ 0.37 (P = 0.001)	- 0.40 (P = 0.002)	n.s.	Imports phosphoenolpyruvate, dihydroxyacetone, and 3-phosphoglycerate across outer apicoplast membrane (134)
V_o c (PF3D7_0519200)	+ 0.36 (P = 0.0006)	n.s.	- 0.16 (P = 0.007)	V-ATPase subunit: active H^+ export from cytosol (135)
MDR1 (PF3D7_0523000)	+ 0.34 (P = 0.0009)	- 0.23 (P = 0.03)	n.s.	Active drug and solute import into DV (136)
NT3 (PF3D7_1469400)	+ 0.34 (P = 0.03)	n.s.	n.s.	Putative nucleoside transporter (36)
SEC61α (PF3D7_1346100)	+ 0.33 (P = 0.0006)	- 0.22 (P = 0.04)	- 0.17 (P = 0.005)	ER import of proteins destined for export (137)
MRS3 (PF3D7_0905200)	+ 0.33 (P = 0.002)	- 0.19 (P = 0.04)	n.s.	Putative Fe^{2+} importer into mitochondrial matrix (38)
HT1 (PF3D7_0204700)	+ 0.33 (P = 0.002)	- 0.30 (P = 0.006)	n.s.	Imports glucose and fructose across PPM (138)
ATP4 (PF3D7_1211900)	+ 0.33 (P = 0.005)	- 0.40 (P = 0.002)	n.s.	H^+ import, Na^+ export across PPM (139)
MCT2 (PF3D7_0926400)	+ 0.32 (P = 0.005)	n.s.	n.s.	Exports organic solutes from apicoplast, imports H^+ (140)
V_1 B (PF3D7_0406100)	+ 0.30 (P = 0.001)	- 0.25 (P = 0.008)	- 0.13 (P = 0.04)	V-ATPase subunit: active H^+ export from cytosol (135)
V_1 A (PF3D7_1311900)	+ 0.30 (P = 0.001)	- 0.28 (P = 0.003)	- 0.20 (P = 0.001)	V-ATPase subunit: active H^+ export from cytosol (135)
TIM16 (PF3D7_0513500)	+ 0.29 (P = 0.03)	n.s.	n.s.	Protein import across inner mitochondrial membrane (131, 141)
VIT (PF3D7_1223700)	+ 0.29 (P = 0.02)	n.s.	n.s.	Fe^{2+} sequestration from cytosol in exchange for H^+ (30-32)
ApiAT2 (PF3D7_0914700)	+ 0.28 (P = 0.006)	n.s.	n.s.	Putative amino acid transporter at PPM (142)
NRAMP (PF3D7_0523800)	+ 0.28 (P = 0.003)	n.s.	n.s.	Symport of Mn^{2+} or Fe^{2+} with H^+ from DV into cytosol (22, 34)
AMC1 (PF3D7_0108800)	+ 0.26 (P = 0.03)	n.s.	n.s.	Putative mitochondrial transporter (143)
CRT (PF3D7_0709000)	+ 0.26 (P = 0.007)	n.s.	n.s.	Symport of positively charged dipeptides or Fe^{2+} with H^+ from DV into cytosol (35)
V_1 H (PF3D7_1306600)	+ 0.26 (P = 0.01)	n.s.	n.s.	V-ATPase subunit: active H^+ export from cytosol (135)
AAC2 (PF3D7_1004800)	+ 0.25 (P = 0.03)	n.s.	- 0.21 (P = 0.04)	Mitochondrial ADP/ATP antiporter (141)
PiT (PF3D7_1340900)	+ 0.24 (P = 0.02)	- 0.21 (P = 0.04)	n.s.	Imports phosphate and Na^+ into cytosol across PPM (36)
V_o d (PF3D7_1464700)	+ 0.24 (P = 0.02)	- 0.23 (P = 0.03)	- 0.15 (P = 0.02)	V-ATPase subunit: active H^+ export from cytosol (135)
V_o c" (PF3D7_1354400)	+ 0.23 (P = 0.03)	n.s.	n.s.	V-ATPase subunit: active H^+ export from cytosol (135)
ATP10 (PF3D7_0727800)	+ 0.23 (P = 0.01)	n.s.	n.s.	Active apicoplast Mn^{2+} transporter (144)
SulP (PF3D7_1471200)	+ 0.23 (P = 0.02)	n.s.	n.s.	Inorganic anion antiporter at PPM (36)
ATP2 (PF3D7_1219600)	+ 0.22 (P = 0.02)	- 0.22 (P < 0.05)	- 0.14 (P = 0.03)	Putative phospholipid flippase at PPM (36)
NT1 (PF3D7_1347200)	+ 0.22 (P = 0.02)	n.s.	n.s.	Purin base import across PPM (145)
AAT1 (PF3D7_0629500)	- 0.26 (P = 0.007)	n.s.	n.s.	Putative amino acid transporter at PPM and DV (143)
MIT1 (PF3D7_1120300)	- 0.27 (P = 0.02)	n.s.	n.s.	Putative mitochondrial magnesium/nickel/cobalt ion channel (141)
AAT2 (PF3D7_1208400)	- 0.29 (P = 0.009)	n.s.	n.s.	Putative amino acid transporter at PPM (36)
MDR7 (PF3D7_1209900)	- 0.34 (P = 0.04)	n.s.	n.s.	Active efflux of peptides from mitochondrion (36, 40)
CuTP (PF3D7_0904900)	- 0.36 (P = 0.008)	+ 0.52 (P = 0.004)	n.s.	Active Cu^{2+} export from cytoplasmic vesicle (36, 146)
GCβ (PF3D7_1360500)	- 0.36 (P = 0.007)	n.s.	n.s.	Putative phospholipid flippase at PPM (36)
TPC (PF3D7_1368700)	- 0.37 (P = 0.01)	+ 0.33 (P = 0.02)	n.s.	Thiamine pyrophosphate import, nucleotide export from mitochondrion (144)
F_1 γ (PF3D7_1311300)	- 0.38 (P = 0.03)	n.s.	+ 0.32 (P = 0.03)	Subunit of mitochondrial H^+-importing ATP synthase (143)

PF3D7_0614900	- 0.43 (*P* = 0.005)	+ 0.72 (*P* = 0.0001)	+ 0.29 (*P* = 0.0003)	Putative ABC transporter at PPM (28)
MFS4 (PF3D7_1203400)	- 0.44 (*P* = 0.0008)	+ 0.56 (*P* = 0.0005)	+ 0.27 (*P* = 0.02)	Putative transporter (36)
F_o d (PF3D7_0311800)	- 0.46 (*P* = 0.004)	+ 0.34 (*P* = 0.02)	n.s.	Subunit of mitochondrial H^+-importing ATP synthase (144)
PF3D7_1004600	- 0.47 (*P* = 0.01)	+ 0.58 (*P* = 0.003)	+ 0.28 (*P* = 0.03)	Putative ABC transporter linked to drug resistance (147)
MPC2 (PF3D7_1470400)	- 0.47 (*P* = 0.03)	+ 0.66 (*P* = 0.005)	n.s.	Subunit of mitochondrial putative pyruvate:H^+ importer (144)
E140 (PF3D7_0104100)	- 0.47 (*P* = 0.03)	+ 0.65 (*P* = 0.006)	n.s.	Putative transport protein at PPM (28)
MDR4 (PF3D7_0302600)	- 0.55 (*P* = 0.001)	+ 0.63 (*P* = 0.001)	+ 0.33 (*P* = 0.02)	Active drug export across innermost apicoplast membrane (148, 149)
ZIPCO (PF3D7_1022300)	- 0.57 (*P* = 0.03)	+ 0.55 (*P* = 0.04)	+ 0.63 (*P* = 0.006)	Zn^{2+}/Fe^{2+} import into cytosol (95)
F_1 δ (PF3D7_1147700)	- 0.59 (*P* = 0.004)	+ 0.63 (*P* = 0.005)	n.s.	Subunit of mitochondrial H^+-importing ATP synthase (143)
TRP-ML (PF3D7_1313500)	- 0.59 (*P* = 0.01)	+ 0.64 (*P* = 0.005)	n.s.	Putative Ca^{2+} channel (150)
F_1 ε (PF3D7_0715500)	- 0.67 (*P* = 0.04)	+ 0.94 (*P* = 0.007)	n.s.	Subunit of mitochondrial H^+-importing ATP synthase (143)
MFS3 (PF3D7_0919500)	- 0.85 (*P* = 0.01)	+ 0.72 (*P* = 0.01)	n.s.	Putative sugar transporter (143)
ATP11 (PF3D7_1468600)	n.s.	+ 1.14 (*P* = 0.005)	n.s.	Putative phospholipid flippase at PPM (28, 36)
NGT (PF3D7_0505300)	n.s.	+ 0.91 (*P* = 0.00008)	+ 0.79 (*P* = 0.00004)	UDP-N-acetylglucosamine import, UMP export from Golgi (36)
SAMC (PF3D7_1241600)	n.s.	+ 0.77 (*P* = 0.03)	+ 0.68 (*P* = 0.02)	S-adenosylmethionine import into mitochondrion (151)
PF3D7_0614900	n.s.	+ 0.72 (*P* = 0.0001)	+ 0.29 (*P* = 0.0003)	Putative active transporter at PPM (28)
GPH (PF3D7_0529200)	n.s.	+ 0.70 (*P* = 0.03)	n.s.	Putative sugar:cation symporter (36)
ATP9 (PF3D7_1348800)	n.s.	+ 0.62 (*P* = 0.04)	n.s.	Active Ca^{2+} import into DV? (144)
CTR2 (PF3D7_1421900)	n.s.	+ 0.52 (*P* = 0.004)	n.s.	Putative apicoplast copper channel (144)
MDR5 (PF3D7_1339900)	n.s.	+ 0.51 (*P* = 0.02)	n.s.	Active solute export across PPM (144)
TIC20 (PF3D7_1144700)	n.s.	+ 0.49 (*P* = 0.007)	n.s.	Protein import across innermost apicoplast membrane (152)
PF3D7_0924500	n.s.	+ 0.47 (*P* = 0.002)	n.s.	Putative Na^+:H^+ exchanger (70)
PPT (PF3D7_0530200)	n.s.	+ 0.46 (*P* = 0.02)		Imports phosphoenolpyruvate, dihydroxyacetone, and 3-phosphoglycerate across inner apicoplast membrane (134)
CLAG3.1 (PF3D7_0302500)	n.s.	+ 0.45 (*P* < 0.05)	n.s.	Purine, amino acid, sugar, and vitamin import across EPM (153)
CDF (PF3D7_0715900)	n.s.	+ 0.44 (*P* = 0.02)	n.s.	Putative Zn^{2+} importer (57) into cytoplasmic vesicles (34)
ATP7 (PF3D7_0319000)	n.s.	+ 0.44 (*P* = 0.007)	n.s.	Putative phospholipid flippase at PPM (28, 36)
RhopH3 (PF3D7_0905400)	n.s.	+ 0.42 (*P* = 0.04)	n.s.	Purine, amino acid, sugar, and vitamin import across EPM (153)
AQP2 (PF3D7_0810400)	n.s.	+ 0.34 (*P* = 0.02)	- 0.19 (*P* < 0.05)	Water channel at PPM (154)
MFS2 (PF3D7_0916000)	n.s.	+ 0.33 (*P* = 0.04)	n.s.	Putative sugar transporter (36)
TFP1 (PF3D7_0206200)	n.s.	+ 0.33 (*P* = 0.02)	n.s.	Putative metabolite transporter at PPM (144)
ATP6 (PF3D7_0106300)	n.s.	- 0.22 (*P* = 0.03)	n.s.	Active Ca^{2+} import into ER for storage (144)
V_1 G (PF3D7_1323200)	n.s.	- 0.23 (*P* = 0.04)	- 0.12 (*P* = 0.04)	V-ATPase subunit: active H^+ export from cytosol (135)
FNT (PF3D7_0316600)	n.s.	- 0.27 (*P* = 0.02)	- 0.16 (*P* = 0.004)	Lactate/formate and H^+ release from cytosol (144)
MFR1 (PF3D7_0614300)	n.s.	- 0.33 (*P* = 0.004)	- 0.14 (*P* = 0.02)	Putative organic anion transporter (36)
PMRT1 (PF3D7_1135300)	n.s.	- 0.36 (*P* = 0.009)	n.s.	Putative transporter at PPM (34)
PLP3 (PF3D7_0923300)	n.s.	- 0.42 (*P* = 0.015)	n.s.	Host cell permeabilization and rupture (128)
OSCP (PF3D7_1310000)	n.s.	n.s.	+ 0.58 (*P* = 0.01)	Subunit of mitochondrial H^+-importing ATP synthase (143)
GFT (PF3D7_0212000)	n.s.	n.s.	+ 0.54 (*P* = 0.03)	GDP-fucose import, GMP export from Golgi (36)
SEC61γ (PF3D7_0210000)	n.s.	n.s.	- 0.23 (*P* = 0.001)	ER import of proteins destined for export (137)
SEC61β (PF3D7_0821800)	n.s.	n.s.	- 0.31 (*P* = 0.0005)	ER import of proteins destined for export (137)
DTC (PF3D7_0823900)	n.s.	n.s.	- 0.34 (*P* = 0.004)	Imports dicarboxylate, exports tricarboxylate from mitochondrion (143)

1295 **Table 2: Proteins identified by RNA-sequencing that may be involved in iron transport in *P. falciparum.***

1296 The classification of the proteins identified is indicated according to the Transport Classification Database (70). Data on human orthologs was retrieved using the NCBI
1297 position-specific iterated (PSI) BLAST with default settings at https://blast.ncbi.nlm.nih.gov/Blast.cgi (29). DV: digestive vacuole, E: expect value, EM: electron microscopy, hpi:
1298 hours post invasion, MIS: mutagenesis index score, PDB: Protein Data Bank, PPM: parasite plasma membrane.

Gene product, gene ID	Blood stage tran-scription peak (47)	Classifi-cation (70)	Solved structure of a similar protein	Potential human ortholog(s)	Localization in *P. falciparum*	Transport assays and proposed function	Mutability in *P. falciparum*	Essentiality in *P. berghei*
MRS3, PF3D7_0905200	20 hpi	2.A.29.5.9	None	Mitoferrin-1 (E = 7 x 10^{-10}, 27.0% identity, 26% coverage); Mitoferrin-2 (E = 6 x 10^{-8}, 27.9% identity, 12% coverage)	Mitochondrion (this study)	Liposomal transport assays with *S. cerevisiae* MRS3 (37): Fe^{2+} import into mitochondrial matrix across inner membrane	Non-disruptable, MIS: 0.135 (64)	PBANKA_041620: essential at asexual blood stage (89)
VIT, PF3D7_1223700	36 hpi	2.A.89.1.13	Crystal structure of VIT1 from *Eucalyptus grandis*: PDB 6IU9 (69)	None	Cytoplasmic vesicles (this study)	Transport assays using inverted vesicles with *Pf*VIT (32): Fe^{2+} export from cytoplasmic vesicles (this study) into cytosol in exchange for H^+	Disruptable, MIS: 0.903 (64)	PBANKA_143860: dispensable at asexual blood stage with growth rate of 1 (95% CI: 0.94 – 1.05) (89), and at mosquito and liver stage (155); reduced growth in blood and liver in mice (30)
ZIPCO, PF3D7_1022300	32 hpi	2.A.5.3.12	Cryo-EM structure of ZIP from *Bordetella bronchiseptica*: PDB 8GHT (71)	ZIP1 (E = 2 x 10^{-5}, 21.7% identity, 48% coverage)	Cytoplasmic vesicles (this study)	Zn^{2+} uptake assays with *Bb*ZIP in *Escherichia coli* (71), Liposomal assays with *Pf*ZIP1 (97): Zn^{2+}/Fe^{2+} import into cytosol from cytoplasmic vesicles (this study)	Disruptable, MIS: 1 (64), growth increase at asexual blood stage (this study)	PBANKA_050650: growth rate of 0.86 (95% CI: 0.74 – 0.98) at asexual blood stage (89); dispensable at blood and mosquito stage but reduced sporozoite infectivity and inefficient schizogony in hepatocytes (95)
NRAMP, PF3D7_0523800	14 hpi	2.A.55.2.25	Crystal structure of NRAMP/DMT from *Staphylo-coccus capitis*: PDB 5M95 (73)	NRAMP1 (E = 2 x 10^{-38}, 28.4% identity, 56% coverage); NRAMP2 (E = 2 x 10^{-38}, 27.6% identity, 65% coverage)	DV (34)	Uptake assays with *Deinococcus radiodurans* NRAMP in *E. coli* and proteoliposomes (99, 100): pH-dependent symport of Mn^{2+}/Fe^{2+} with H^+ into cytosol from DV	Non-disruptable, MIS: 0.123 (64)	PBANKA_123860: no mutants generated
CRT, PF3D7_0709000	14 hpi	2.A.7.20.1	Cryo-EM structure of *Pf*CRT from strain 7G8: PDB 6UKJ (72)	None	DV (60)	Transport assays using *Xenopus* oocytes with *Pf*CRT (35): symport of Fe^{2+} with H^+ into cytosol from DV	Non-disruptable, MIS: 0.127 (64), essential at asexual blood stage	PBANKA_121950: essential at asexual blood stage (89, 156)

							(33)	
E140, PF3D7_0104100	40 hpi	Unknown	None	None	PPM (this study)	Putative Fe^{2+} importer at PPM (this study)	Non-disruptable, MIS: 0.119 (64)	PBANKA_0209000: growth rate of 0.48 (95% CI: 0.32 – 0.63) at asexual blood stage (89), dispensable in mosquito and liver stages (155)

Supplementary Material

mentary Figures

Supplementary Figure S1: RNA quality.

Supplementary Figure S2: Cloning strategy and confirmation of correct DNA integration into the genome of the cell lines generated.

Supplementary Figure S3: Sequence alignments of *P. falciparum* proteins with their potential orthologs from other species that have been functionally characterized.

Supplementary Figure S4: Alignments of functional sites in the predicted *P. falciparum* protein structures with those of potential orthologs using UCSF Chimera.

Supplementary Videos

Supplementary Video S1: Parasite endogenously expressing *Pf*MRS3-GFP stained with MitoTracker Red and Hoechst-33342.

Supplementary Video S2: Parasite endogenously expressing *Pf*VIT-GFP stained with ER Tracker Red and Hoechst-33342.

Supplementary Video S3: Parasite endogenously expressing *Pf*ZIPCO-GFP stained with LysoTracker Deep Red and Hoechst-33342.

Supplementary Video S4: Parasite expressing *Pf*E140-GFP endogenously, *Pf*ACP(1-60)-mCherry episomally and stained with Hoechst-33342.

Supplementary Tables

Supplementary Table S1: Differentially expressed genes of *P. falciparum* 3D7 cultured with erythrocytes from a donor with high, control or low iron status.

Supplementary Table S2: Differentially expressed genes of *P. falciparum* 3D7 cultured with erythrocytes from a healthy donor with or without addition of 0.7 µM hepcidin.

Supplementary Table S3: Oligonucleotides (A) and plasmids (B) used in this study.

Supplementary PDB files

Top-scoring PDB files for the multimers that were computed at EMBL:

PfVIT.pdb

PfZIPCO.pdb

Funding

This work was supported by a Boehringer Ingelheim Foundation Exploration Grant, the Partnership for Innovation, Education and Research (PIER) of Hamburg University and DESY (project PIF-2018-87) and the European Molecular Biology Laboratory (EMBL). JW was additionally funded by the European Research Council under the European Union's

Horizon 2020 Research and Innovation Programme (grant agreement 759534) and VK by a research fellowship from the EMBL Interdisciplinary Postdoc (EIPOD) Programme under Marie Curie Cofund Actions MSCA-COFUND-FP (grant agreement 847543). The funders had no role in study design, data collection and analysis, decision to publish, or preparation of the manuscript.

Authors' contributions

JS and JW designed the study; MG and SPe recruited the blood donors; JW and CN performed the experiments; JW, JS, VK and LVN analyzed the data; VK generated the structural models, and JW wrote the manuscript with contributions from VK, JS and SPo. All authors read and approved the submitted version.

Acknowledgements

The authors thank the Genomics Core Facility at EMBL Heidelberg, especially Vladimir Benes, for the RNA-sequencing service, and EMBL Hamburg for the provision of research and technical support as well as access to research infrastructures. Grzegorz Chojnowski and the group of Jan Kosinski at EMBL Hamburg enabled the AlphaFold2 workflow at the EMBL Hamburg computer cluster. The Advanced Light and Fluorescence Microscopy Facility at CSSB Hamburg, in particular Roland Thünauer, supported microscopy experiments, and the Bernhard Nocht Institute for Tropical Medicine (BNITM) provided lab space. We gratefully acknowledge Tobias Spielmann for pSLI-GFP and pARL-*Pf*ACP(1-60)-mCherry, Paul Burda for pSLI-GFP-*glmS*, Jacobus Pharmaceuticals for WR99210, Anna Bachmann and Mayka Sánchez for helpful advice, Eileen Devaney, Katharina Jungnickel, and Samuel Pažický for critical reading of the manuscript, and Heidrun von Thien, Yannick Höppner, and Gabriela Guédez for technical assistance.

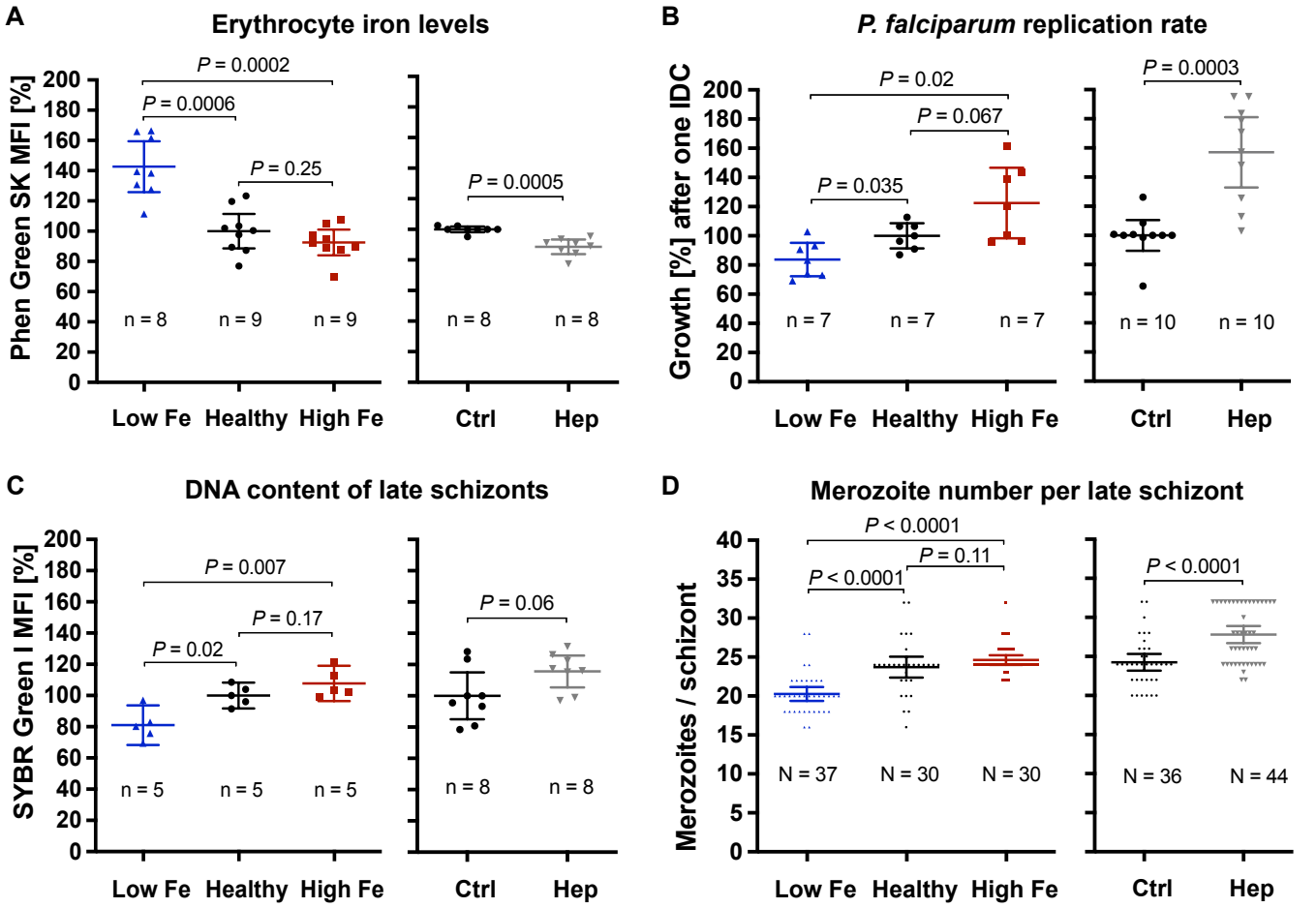

Figure 1: Effects of the iron status of the blood donor and of hepcidin on (A) erythrocyte free iron levels, (B) *P. falciparum* 3D7 growth rates, (C) DNA content per mature schizont, and (D) the number of merozoites per mature schizont.

The relative free iron level and DNA content per cell were assessed by measuring the mean fluorescence intensity (MFI) of Phen Green SK or SYBR Green I compared to control (Ctrl, untreated, normal hemoglobin level) using flow cytometry. 0.7 µM hepcidin (Hep) was chosen as a concentration reported to reduce binding of ferrous iron to the erythrocyte iron exporter ferroportin by 50% in vitro (44). Parasite growth rates refer to the fold change in parasitemia after one intraerythrocytic developmental cycle in vitro relative to control as determined by flow cytometry with SYBR Green I (103). Mature schizonts were obtained by treating schizonts at 40 hpi with 1 mM compound 2 (4-[7-[(dimethylamino)methyl]-2-(4-fluorphenyl)imidazo[1,2-α]pyridine-3-yl]pyrimidin-2-amine) for 8 h. To count the number of merozoites, Giemsa-stained blood smears were analyzed microscopically and only single-infected cells with one digestive vacuole were considered. Means and 95% confidence intervals (indicated by error bars) are shown. Statistical significance was calculated with two-tailed unpaired t tests with Welch's correction for unequal variances and adjusted with the Holm-Šídák method for multiple comparisons except for merozoite numbers, which were compared using Mann-Whitney test. N represents the number of parasites and n the number of independent experiments.

A

	Experiment 1			Experiment 2	
	Low Fe	**Healthy control**	**High Fe**	**Hepcidin-treated**	**Untreated control**
MLE of parasite age [hpi] at ring stage	9.9 (97.5% CI: 9.6 – 10.3)	10.2 (97.5% CI: 9.8 – 10.7)	10.0 (97.5% CI: 9.6 – 10.5)	10.2 (97.5% CI: 9.8 – 10.7)	10.6 (97.5% CI: 10.2 – 11.0)
MLE of parasite age [hpi] at trophozoite stage	35.4 (97.5% CI: 34.8 – 35.8)	35.5 (97.5% CI: 35.0 – 36.0)	35.4 (97.5% CI: 34.8 – 36.0)	34.7 (97.5% CI: 34.0 – 35.3)	34.5 (97.5% CI: 33.8 – 35.0)

B

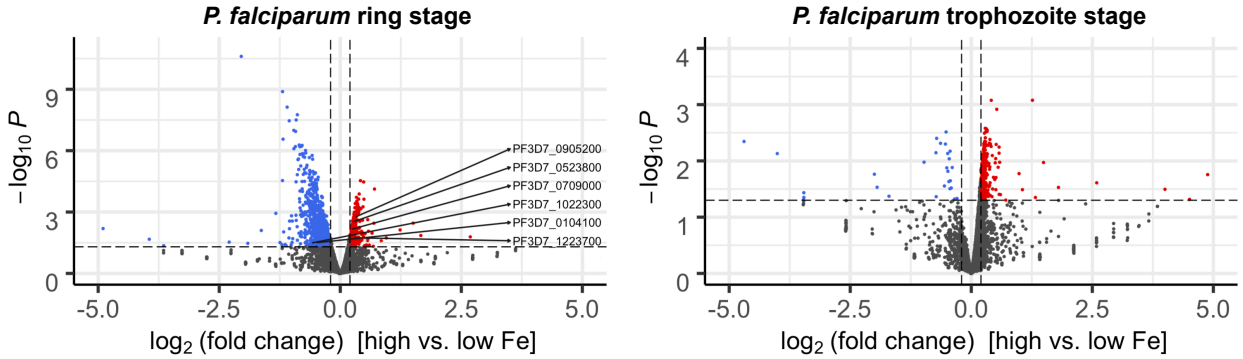

C

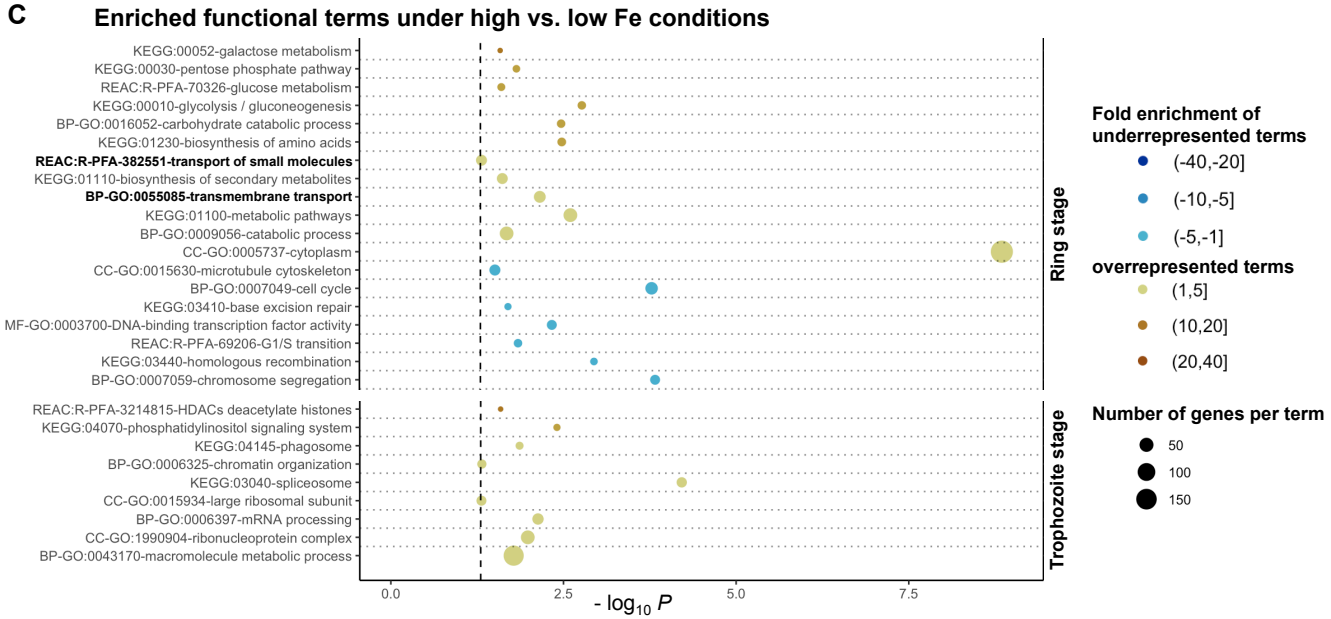

D

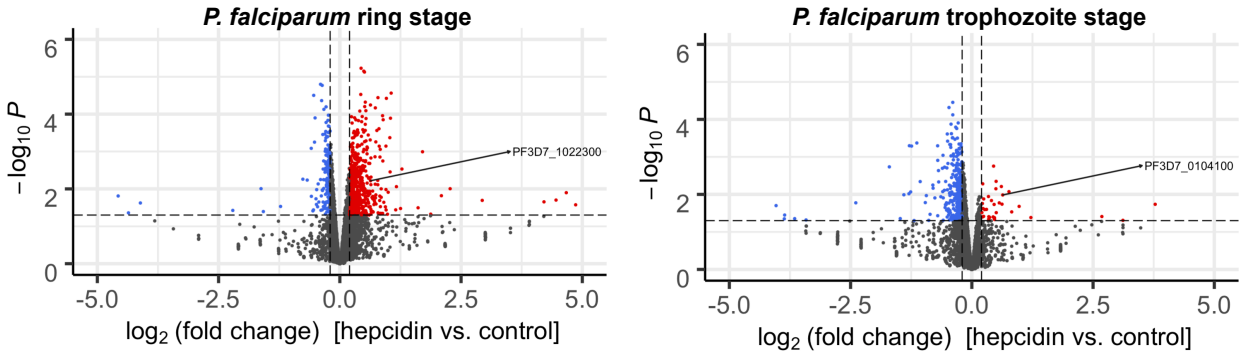

E

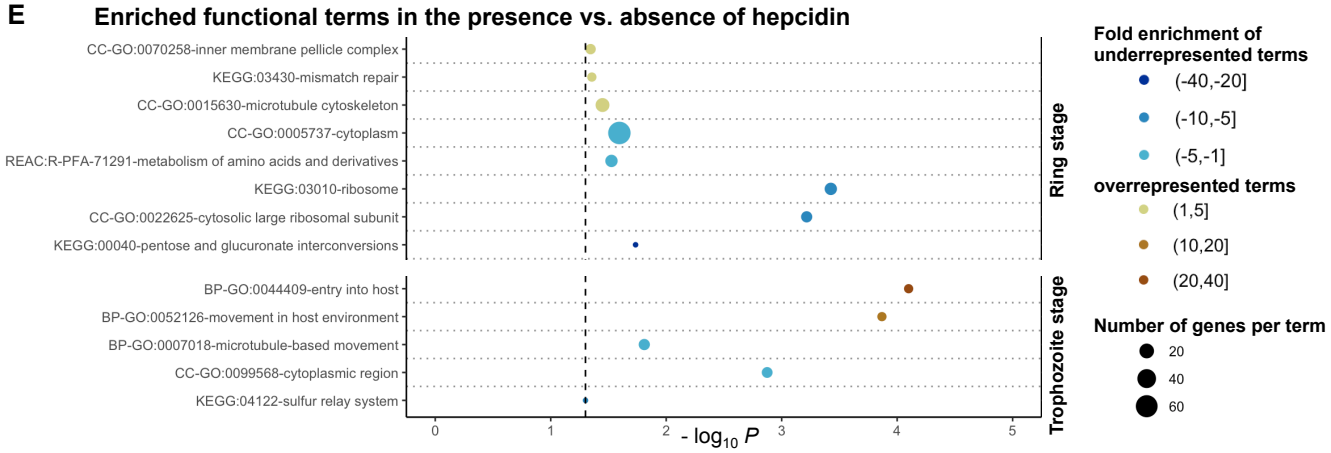

Figure 2: Differential expression of *P. falciparum* 3D7 genes under various iron conditions. Parasites were cultured with erythrocytes from an individual with high, medium (healthy) or low iron status (experiment 1) or with red blood cells from another healthy donor in the presence or absence of 0.7 µM hepcidin (experiment 2). Samples were harvested at the ring and trophozoite stage (6 – 9 and 26 – 29 hours post invasion, hpi) with three biological replicates per time point and condition. The maximum likelihood estimation (MLE) of the average developmental age of the parasites for each condition and time point (**A**) was calculated using an algorithm developed by Avi Feller and Jacob Lemieux (46). CI, confidence interval. The volcano plots (**B** and **D**) show transcriptional changes of all parasite genes. Red dots indicate significantly ($P < 0.05$, exact test for negative binomial distribution) upregulated genes ($\log_2$ (fold change) ≥ 0.2), blue dots stand for significantly downregulated genes ($\log_2$ (fold change) ≤ -0.2), while grey dots represent genes that did not significantly differ in transcription under the conditions described ($P \geq 0.05$ and / or $-0.2 < \log_2$ (fold change) < 0.2). Differentially expressed genes encoding putative iron transporters (see Table 1) are labeled. Panels **C** and **E** show the enrichment of Gene Ontology (GO), Kyoto Encyclopedia of Genes and Genomes (KEGG) and Reactome (REAC) terms among significantly regulated genes excluding *var*, *stevor* and *rifin* gene families at the two time points. The functional terms were summarized using REVIGO (121) to remove redundancies, represented by circles and plotted according to the significance of their enrichment ($-\log_{10}$ (adjusted P), hypergeometric test). The size of the circle is proportional to the number of differentially regulated genes in the dataset that are associated with the respective term, while the color stands for the fold enrichment. The gray dashed line indicates the threshold of the adjusted P value ($-\log_{10} 0.05 = 1.3$).

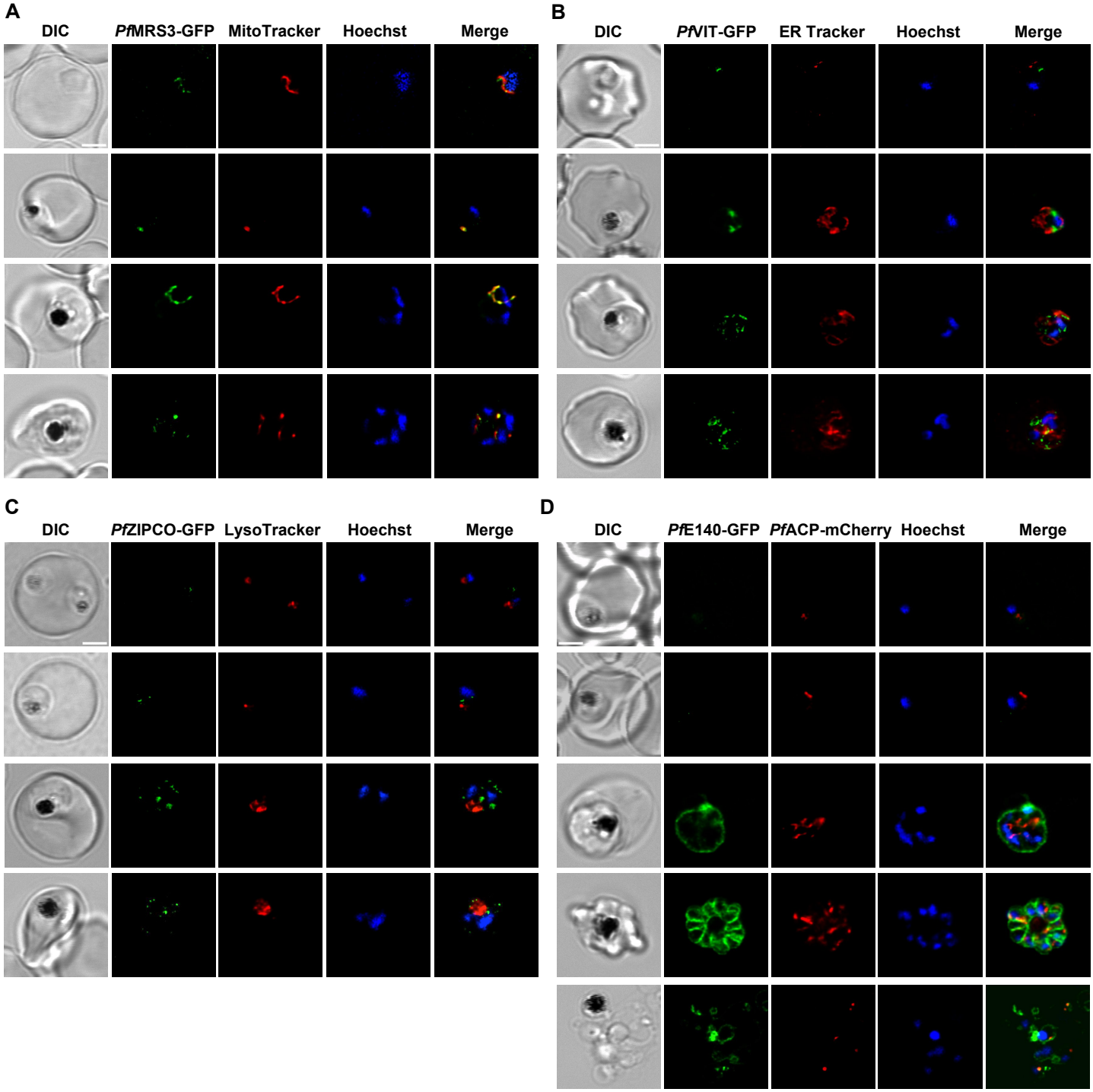

Figure 3: Subcellular localization of four putative iron transport proteins.
Representative erythrocytes infected with *P. falciparum* 3D7 parasites endogenously expressing GFP-tagged *Pf*MRS3 (**A**), *Pf*VIT (**B**), *Pf*ZIPCO (**C**) or *Pf*E140 (**D**) were additionally stained with the fluorescent dyes Hoechst-33342, MitoTracker Red, ER Tracker Red and/or LysoTracker Deep Red. Co-transfection with a construct that encodes the 60 N-terminal amino acids of acyl carrier protein (*Pf*ACP) tagged with mCherry (125) resulted in red fluorescence of the apicoplast. Live-cell images were taken under physiological conditions at 37°C using an SP8 confocal laser-scanning microscope (Leica). DIC, differential interference contrast. Scale bar, 2 µm.

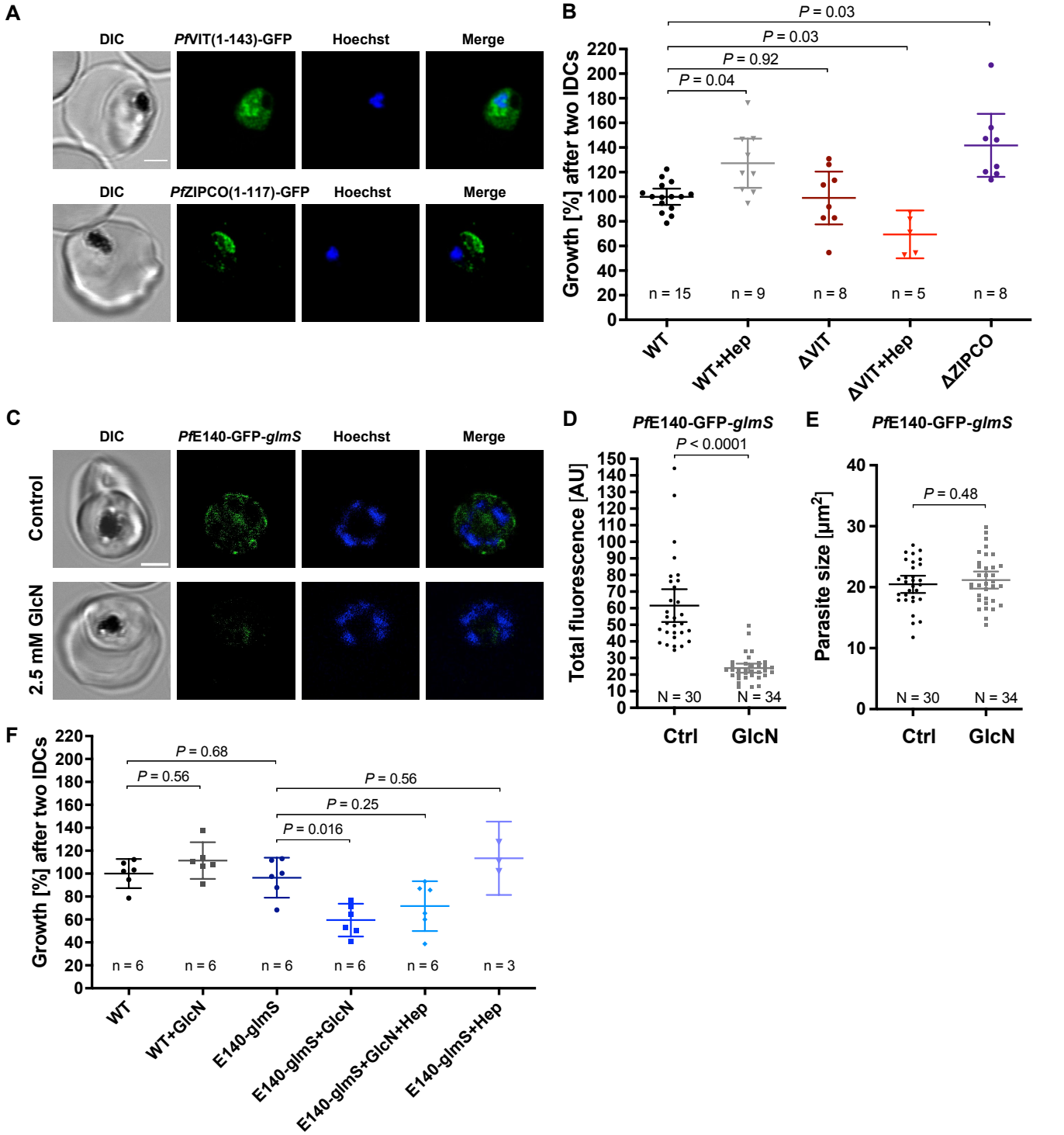

Figure 4: *Pf*VIT and *Pf*E140 are important for *P. falciparum* growth and may be involved in intracellular iron homeostasis.

A Representative erythrocytes infected with *P. falciparum* 3D7 parasites that endogenously express a truncated version of *Pf*VIT or *Pf*ZIPCO tagged with GFP (green). **B** Growth rates of knockout parasite lines generated. **C** Reduction of *Pf*E140-GFP fluorescence (green) in live 3D7 parasites caused by *glmS*-mediated knockdown that was induced by treatment with 2.5 mM glucosamine (GlcN) for 36 h compared to untreated control (Ctrl). **D** Total parasite fluorescence intensities were quantified as background-corrected integrated densities using ImageJ version 2.9.0/1.53t (109) and compared using Mann-Whitney test. **E** The size of the parasites was measured as the area of the region of interest and compared using equal variance unpaired t test. **F** Conditional knockdown of *Pf*E140 induced by treatment with 2.5 mM GlcN results in a growth defect during asexual blood stage development. Live parasites were stained with Hoechst-33342 (blue) and imaged under physiological conditions at 37°C using an SP8 confocal laser-scanning microscope (Leica). DIC, differential interference contrast. Scale bar, 2 µm. Error bars represent 95% confidence intervals of the mean, N the number of parasites analyzed, n the number of independent experiments and Hep treatment with 0.7 µM hepcidin. Growth rates refer to the fold change in parasitemia after two intraerythrocytic developmental cycles in vitro relative to untreated wild-type 3D7 parasites (WT) as determined by flow cytometry with SYBR Green I (103). Statistical significance of growth differences was calculated with two-tailed unpaired t tests with Welch's correction for unequal variances and adjusted with the Holm-Šídák method for multiple comparisons.

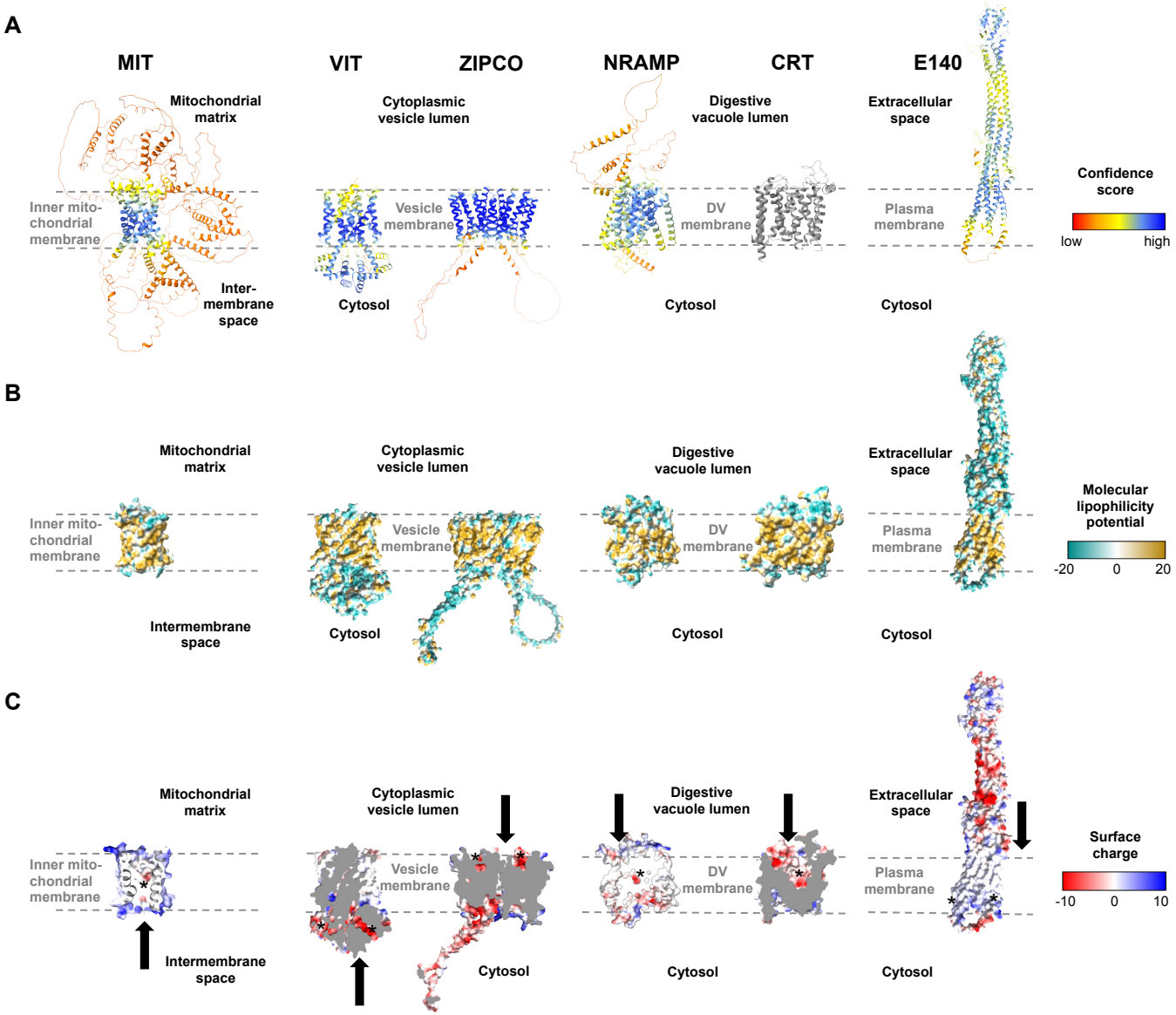

Figure 5: Predicted structures of putative iron transporters identified in P. falciparum as viewed from the membrane plane.
A Predicted protein structures with per-residue pLDDT (predicted local distance difference test) confidence scores on a scale from 0 to 100, where blue represents high and red low confidence, respectively. The experimentally determined structure of *Pf*CRT is shown in gray. **B** Molecular lipophilicity potential of the protein surfaces as implemented in UCSF ChimeraX; tan is hydrophobic and cyan hydrophilic. Dashed lines above and below the tan regions of all proteins indicate the respective membrane and disordered loops were removed for clarity. **C** Surface charge of the proteins with positively charged areas colored blue and negatively charged ones red. Putative cation-binding site are indicated with an asterisk and transport directions by arrows. *Pf*E140 likely forms a dimer but is shown as a monomer, as no predicted dimer structure could be obtained using AlphaFold2-multimer. The putative cation-binding sites for this protein are based on DeepFRI gradCAM scores for the functional term GO:0015075 “monoatomic ion transmembrane transporter activity” (Supplementary Fig. S5).

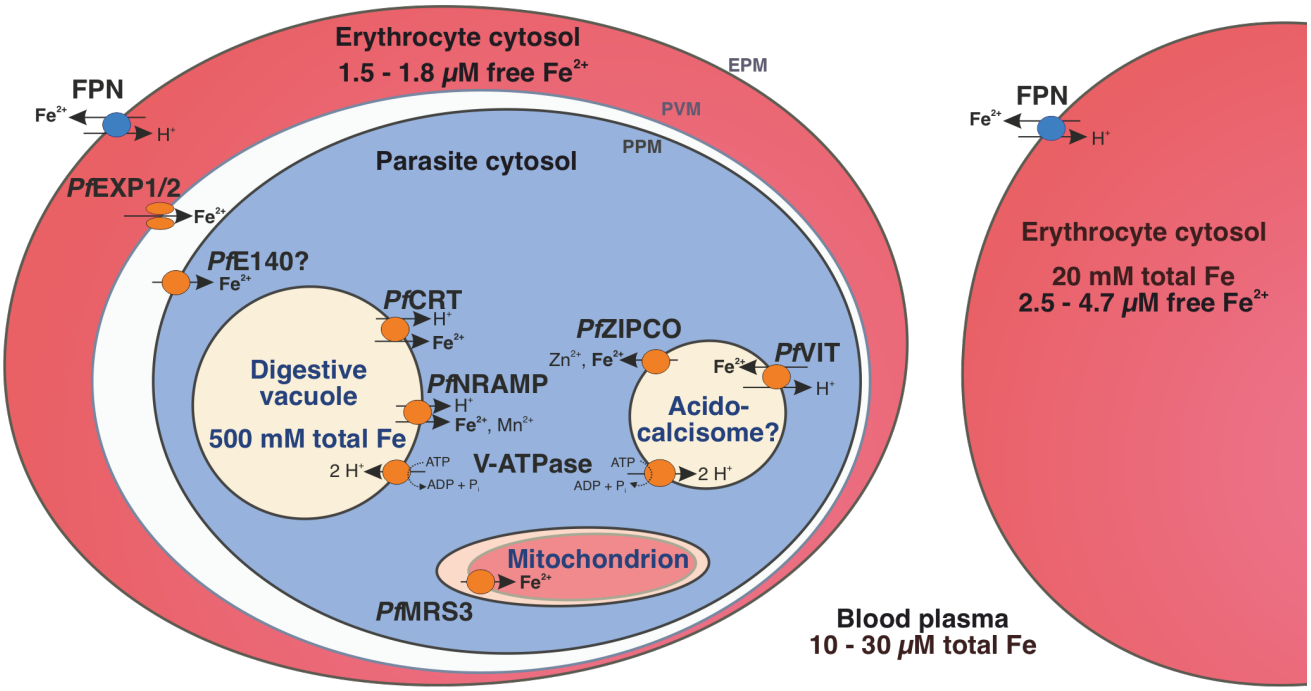

Figure 6: Iron homeostasis in a *P. falciparum*-infected erythrocyte.
The human blood plasma contains between 10 and 30 μM total Fe and the erythrocyte cytosol approximately 20 mM (19). However, only 2.5 – 4.7 μM of Fe^{2+} is bioavailable in an uninfected erythrocyte, and 1.5 – 1.8 μM in a *P. falciparum*-infected one (20). Human ferroportin (FPN) at the host cell surface (erythrocyte plasma membrane, EPM) exports free iron from the erythrocyte (126), the nutrient pore formed by *Pf*EXP1 and *Pf*EXP2 allows the passage of the ions through the parasitophorous vacuole membrane (PVM) (127). *Pf*E140 at the parasite plasma membrane (PPM) may mediate iron uptake iron into the parasite cytosol and the mitochondrial carrier protein *Pf*MRS3 likely translocates Fe^{2+} into the mitochondrion, a site of *de novo* heme biosynthesis. The digestive vacuole (DV) contains a high amount of total Fe as it is the site of hemoglobin degradation. The chloroquine resistance transporter (*Pf*CRT) and the natural resistance-associated macrophage protein (*Pf*NRAMP) were suggested to mediate proton-coupled export of Fe^{2+} from the DV into the parasite cytosol (35, 36). The vacuolar iron transporter (*Pf*VIT) may be involved in iron detoxification by transporting excess iron from the cytosol into cytoplasmic vesicles that may be acidocalcisomes, whereas *Pf*ZIPCO may release zinc and ferrous iron from these organelles under low-iron conditions (this study). Both acidocalcisomes and the DV are likely acidified by the plant-like H^+-pump V-ATPase, which can fuel secondary active transport processes (22, 27). Parasite-encoded proteins are shown in orange and human-encoded transporters in blue.